Production mechanism of hidden-charm pentaquark states $P_{c\bar{c}s}$ with strangeness $S = -1$

Samson Clymton,[1,2,*] Hyun-Chul Kim,[1,3,†] and Terry Mart[4,‡]

[1]*Department of Physics, Inha University, Incheon 22212, Republic of Korea*
[2]*Asia Pacific Center for Theoretical Physics (APCTP), Pohang, Gyeongbuk 37673, Republic of Korea*
[3]*School of Physics, Korea Institute for Advanced Study (KIAS), Seoul 02455, Republic of Korea*
[4]*Departemen Fisika, FMIPA, Universitas Indonesia, Depok 16424, Indonesia*

(Received 11 April 2025; accepted 24 June 2025; published 28 July 2025)

We investigate the hidden-charm pentaquark states with strangeness $S = -1$ ($P_{c\bar{c}s}$) within an off shell coupled-channel approach based on effective Lagrangians that respect heavy-quark spin symmetry, SU(3) flavor symmetry, and hidden local symmetry. All relevant meson-baryon two-body channels composed of low-lying anticharmed mesons and singly charmed baryons with $S = -1$, as well as the $J/\psi\Lambda$ channel, are included. We find a total of 11 negative-parity states and three positive-parity states. Among the negative-parity states, the $P_{c\bar{c}s}(4338)$ and $P_{c\bar{c}s}(4459)$ can possibly be interpreted as $\bar{D}\Xi_c$ and $\bar{D}^*\Xi_c$ molecular states, respectively. We identify a second state, $P_{c\bar{c}s}(4472)$, located close to the $P_{c\bar{c}s}(4459)$ but with different spin and width, which may correspond to the structure observed by the Belle Collaboration. Both states are generated from the $\bar{D}^*\Xi_c$ channel and can be interpreted as spin partners. Their properties are consistent with recent experimental observations, providing strong support for the molecular interpretation of the $P_{c\bar{c}s}$ states. We also observe a two-pole structure near the $\bar{D}_s^*\Lambda_c$ and $\bar{D}\Xi_c'$ thresholds, and find virtual and resonance states in the $\bar{D}^*\Xi_c'$ channel depending on spin-parity.

DOI: 10.1103/2wvg-jlxp

I. INTRODUCTION

Since the observation of five hidden-charm pentaquark states [1–3], there has been a great deal of experimental and theoretical work on these heavy-pentaquark states. Subsequently, the LHCb Collaboration reported the existence of a neutral hidden-charm pentaquark with strangeness, denoted as $P_{c\bar{c}s}(4459)$. The initial observation was made in the $J/\psi\Lambda$ invariant mass spectrum from the $\Xi_b^- \to J/\psi\Lambda K^-$ decay, revealing the $P_{c\bar{c}s}(4459)$ state with mass $M_{P_{c\bar{c}s}} = (4458.8 \pm 2.9^{+4.7}_{-1.1})$ MeV$/c^2$ and width $\Gamma = (17.3 \pm 6.5^{+8.0}_{-5.7})$ MeV [3]. A second state, $P_{c\bar{c}s}(4338)$, was identified in the $J/\psi\Lambda$ invariant mass spectrum from the $B^- \to J/\psi\Lambda\bar{p}$ decay, with mass $M_{P_{c\bar{c}s}} = (4338.2 \pm 0.7 \pm 0.4)$ MeV$/c^2$ and width $\Gamma = (7.0 \pm 1.2 \pm 1.3)$ MeV [4]. Its spin-parity quantum numbers were successfully determined to be $J^P = 1/2^-$. These observations provide compelling evidence for the existence of pentaquark states. Very recently, the Belle Collaboration confirmed the existence of $P_{c\bar{c}s}(4459)$, but reported a slightly larger mass: $M_{P_{c\bar{c}s}} = (4471.7 \pm 4.8 \pm 0.6)$ MeV$/c^2$ and decay width $\Gamma = (21.9 \pm 13.1 \pm 2.7)$ MeV [5]. Considering that the Compact Muon Solenoid and LHCb collaborations have respectively reported the measurements of $\Lambda_b^0 \to J/\psi\Xi^- K^+$ and $\Xi_b^0 \to J/\psi\Xi^-\pi^+$ decays, one may anticipate the possible existence of $S = -2$ hidden-charm pentaquark states in the near future, denoted as $P_{c\bar{c}ss}$ [6,7].

Before the discovery of hidden-charm pentaquarks with strangeness $S = -1$, they had been predicted as molecular states composed of a heavy meson and a singly heavy baryon system [8–10]. This interpretation was supported by experimental observations, in which the mass of the $P_{c\bar{c}s}$ state was found to be lower than the threshold energy of certain heavy meson-heavy baryon systems. Moreover, the molecular nature of these states has been extensively investigated within various theoretical frameworks [11–16]. However, alternative interpretations of the $P_{c\bar{c}s}$ states have also been proposed, including compact pentaquark configurations [17–19], or even kinematical effects [20]. Thus, it is of great importance to investigate and understand the nature of the newly observed $P_{c\bar{c}s}$ states within various theoretical frameworks.

In our previous work, we successfully studied the production of nonstrange hidden-charm pentaquark states

*Contact author: samson.clymton@apctp.org
†Contact author: hchkim@inha.ac.kr
‡Contact author: terry.mart@sci.ui.ac.id

Published by the American Physical Society under the terms of the Creative Commons Attribution 4.0 International license. Further distribution of this work must maintain attribution to the author(s) and the published article's title, journal citation, and DOI. Funded by SCOAP³.

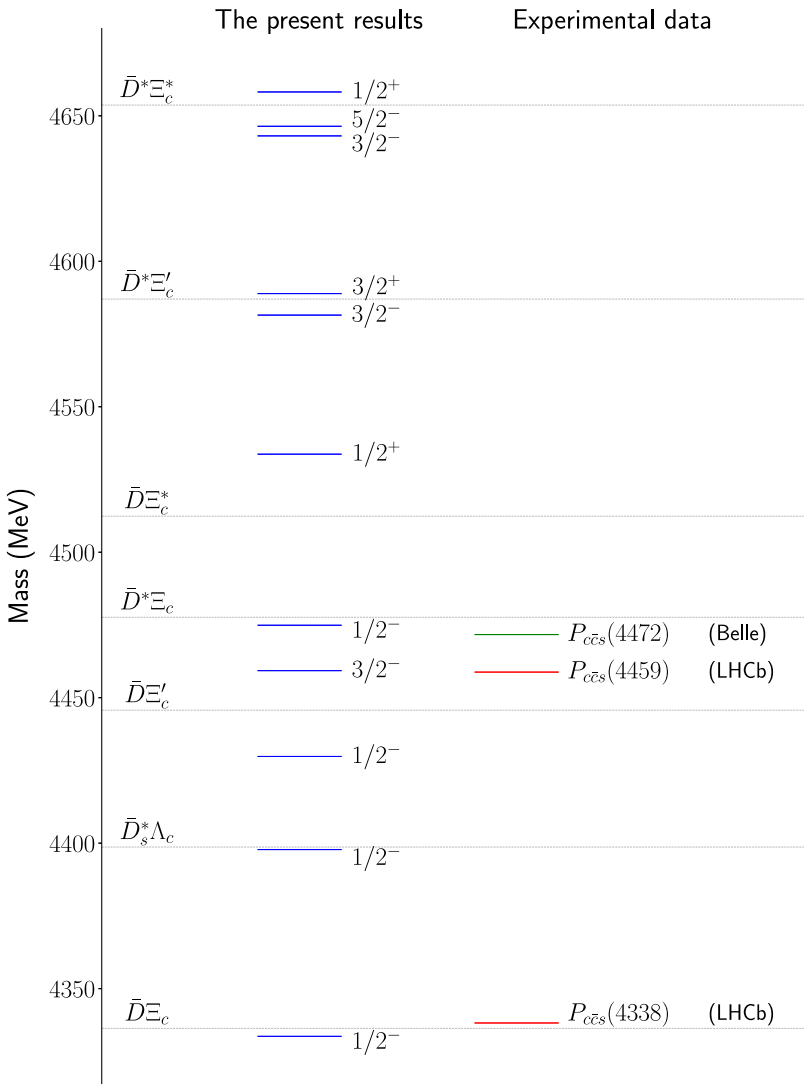


FIG. 1. Mass spectrum of the $P_{c\bar{c}s}$'s, obtained from the present work. The experimental data are taken from the LHCb [3,4] and Belle [5] measurements, respectively.

from meson-baryon scattering using an off shell coupled-channel approach [21]. We first constructed the kernel Feynman amplitudes for the relevant channels based on an effective Lagrangian that respects heavy-quark spin-flavor symmetry, hidden local symmetry, and chiral symmetry. We then solved the coupled-channel scattering integral equation involving seven different coupled channels. By searching for poles corresponding to hidden-charm pentaquark states in the complex energy plane, we found four hidden-charm pentaquark states with negative parity, which were associated with the $P_{c\bar{c}}$ states observed by the LHCb Collaboration: $P_{c\bar{c}}(4312)$, $P_{c\bar{c}}(4380)$, $P_{c\bar{c}}(4440)$, and $P_{c\bar{c}}(4457)$. In addition, we predicted the existence of two further negative-parity and two positive-parity $P_{c\bar{c}}$ states.

Moreover, we provided an explanation for the absence of a $P_{c\bar{c}}$ signal in the $J/\psi N$ photoproduction reported by the GlueX experiment [22]: destructive interference in the $J/\psi N$ scattering, combined with suppression due to a dominant positive-parity contribution, leads to the weakening of hidden-charm pentaquark signals in the $J/\psi N$ channel [21].

In the present work, we extend this approach to investigate hidden-charm pentaquark states with strangeness $S=-1$, introducing the relevant heavy meson-heavy baryon scattering channels. As a result, we have found eight resonances with negative parity and three with positive parity for spin $1/2$, $3/2$, and $5/2$. Two of these can be associated with the experimentally observed $P_{c\bar{c}s}$ states: $P_{c\bar{c}s}(4338)$ and $P_{c\bar{c}s}(4459)$. Figure 1 summarizes the results for the predictions of the $P_{c\bar{c}s}$ pentaquarks obtained from the current work. The remaining nine pentaquark states are considered predictions. We want to emphasize that the *two* hidden-charm pentaquark states below the $\bar{D}^*\Xi_c$ threshold should be different ones with different spins.

The present work is organized as follows: in Sec. II, we present the theoretical formalism employed to investigate hidden-charm strange pentaquarks, incorporating all possible two-body channels composed of ground-state charmed baryons and anticharmed mesons, along with the additional $J/\psi\Lambda$ channel. The resulting scattering matrix is analyzed by examining its behavior in both the real and complex energy domains. In Sec. III, we discuss our findings, with particular focus on the molecular nature of each resonant state. Finally, we conclude the paper with a summary and concluding remarks in Sec. IV.

II. COUPLED-CHANNEL FORMALISM

The scattering amplitude is defined as

$$\mathcal{S}_{fi} = \delta_{fi} - i(2\pi)^4\delta(P_f - P_i)\mathcal{T}_{fi}, \tag{1}$$

where P_i and P_f denote the total four-momenta of the initial and final states, respectively. The transition amplitudes $\mathcal{T}_{fi}$ are obtained from the Bethe-Salpeter integral equation with the two-body Feynman kernel amplitudes

$$\begin{aligned}\mathcal{T}_{fi}(p', p; s) = \mathcal{V}_{fi}(p', p; s) \\ + \frac{1}{(2\pi)^4}\sum_k \int d^4q \mathcal{V}_{fk}(p', q; s)\mathcal{G}_k(q; s) \\ \times \mathcal{T}_{ki}(q, p; s),\end{aligned} \tag{2}$$

where p and p' indicate the relative four-momenta of the initial and final states, respectively. q represents the off-mass-shell momentum for the intermediate states in the c.m. frame. s is the square of the total energy, which is one of the Mandelstam variables, $s = P_i^2 = P_f^2$. The coupled integral equations presented in Eq. (2) can be visualized as shown in Fig. 2.

To reduce the complexity of the four-dimensional integral equations, we implement a three-dimensional reduction. Among various methods for three-dimensional reduction, we utilize the Blankenbecler-Sugar formalism [23,24], which expresses the two-body propagator in the form of

$$\begin{aligned}\mathcal{G}_k(q) = \delta\left(q_0 - \frac{E_{k1}(\boldsymbol{q}) - E_{k2}(\boldsymbol{q})}{2}\right) \\ \times \frac{\pi}{E_{k1}(\boldsymbol{q})E_{k2}(\boldsymbol{q})}\frac{E_k(\boldsymbol{q})}{s - E_k^2(\boldsymbol{q})},\end{aligned} \tag{3}$$

where E_k is the total on-mass-shell energy of the intermediate state, $E_k = E_{k1} + E_{k2}$, and $\boldsymbol{q}$ denotes the three-momentum of the intermediate state. Note that the spinor contributions from the meson-baryon propagator G_k have been incorporated into the matrix elements of $\mathcal{V}$ and $\mathcal{T}$. By applying Eq. (3), we derive the following coupled integral equations:

$$\begin{aligned}\mathcal{T}_{fi}(\boldsymbol{p}', \boldsymbol{p}) = \mathcal{V}_{fi}(\boldsymbol{p}', \boldsymbol{p}) + \frac{1}{(2\pi)^3}\sum_k \int \frac{d^3q}{2E_{k1}(\boldsymbol{q})E_{k2}(\boldsymbol{q})} \\ \times \mathcal{V}_{fk}(\boldsymbol{p}', \boldsymbol{q})\frac{E_k(\boldsymbol{q})}{s - E_k^2(\boldsymbol{q}) + i\varepsilon}\mathcal{T}_{ki}(\boldsymbol{q}, \boldsymbol{p}),\end{aligned} \tag{4}$$

where $\boldsymbol{p}$ and $\boldsymbol{p}'$ are the relative three-momenta of the initial and final states in the c.m. frame, respectively.

To investigate the dynamical generation of the pentaquark states with strangeness $S = -1$, we construct two-body coupled channels by combining the charmed meson triplet with the singly charmed baryon antitriplet and sextet, selecting only the combinations that yield strangeness $S = -1$. In addition, we include the $J/\psi\Lambda$ channel, as the $P_{c\bar{c}s}$ states have been experimentally observed to decay into $J/\psi\Lambda$. This results in nine distinct channels with $S = -1$: $J/\psi\Lambda$, $\bar{D}_s\Lambda_c$, $\bar{D}\Xi_c$, $\bar{D}_s^*\Lambda_c$, $\bar{D}\Xi_c'$, $\bar{D}^*\Xi_c$, $\bar{D}\Xi_c^*$, $\bar{D}^*\Xi_c'$, and $\bar{D}^*\Xi_c^*$. We construct the kernel matrix using one-meson exchange tree-level diagrams, as illustrated in Fig. 3. In our approach, we exclude any pole diagrams in the s-channel, since we want to demonstrate how the hidden-charm pentaquark states are generated dynamically by the interplay between various coupled channels. Nevertheless, we want to mention the importance of the s-channel pole diagrams in describing existing resonances. There will be certain contributions from them, so that the pole positions and widths of the $P_{c\bar{c}s}$'s may be influenced by them. However, it is of great difficulty to consider them without additional uncertainties involved, in particular, when the predicted $P_{c\bar{c}s}$'s are concerned. Thus, our primary focus is on the t-channel diagrams, which play a crucial role in dynamically generating the $P_{c\bar{c}s}$ states. The u-channel diagrams contain the exchange of doubly charmed baryons with masses around 3.5 GeV and are significantly suppressed in magnitude compared to the t-channel diagrams. As a result, their contributions are negligible, and we therefore omit them from our analysis.

The vertex interactions are determined by an effective Lagrangian that respects heavy-quark spin symmetry, hidden local symmetry, and flavor SU(3) symmetry [25].

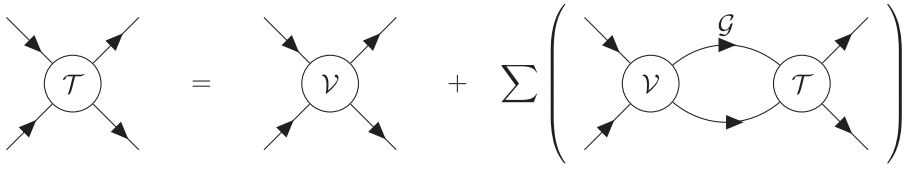


FIG. 2. Graphical representation of the coupled integral scattering equation with the two-body intermediate states.

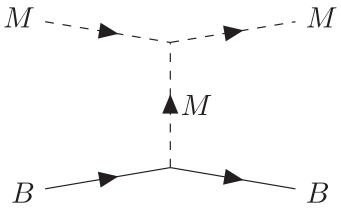


FIG. 3. t-channel diagrams for the meson-exchanged diagrams. M and B stand for the meson and baryon, respectively.

The mesonic vertices are computed using the effective Lagrangian given by

$$\mathcal{L}_{PP\mathbb{V}} = -i\frac{\beta g_V}{\sqrt{2}} P_a^\dagger \overleftrightarrow{\partial}_\mu P_b \mathbb{V}^\mu_{ba} + i\frac{\beta g_V}{\sqrt{2}} P'^\dagger_a \overleftrightarrow{\partial}_\mu P'_b \mathbb{V}^\mu_{ab}, \quad (5)$$

$$\mathcal{L}_{PP\sigma} = -2g_\sigma M P_a^\dagger \sigma P_a - 2g_\sigma M P'^\dagger_a \sigma P'_a, \quad (6)$$

$$\mathcal{L}_{P^*P^*\mathbb{P}} = -\frac{g}{f_\pi}\epsilon^{\mu\nu\alpha\beta} P^{*\dagger}_{a\nu} \overleftrightarrow{\partial}_\mu P^*_{b\beta} \partial_\alpha \mathbb{P}_{ba} - \frac{g}{f_\pi}\epsilon^{\mu\nu\alpha\beta} P'^{*\dagger}_{a\nu} \overleftrightarrow{\partial}_\mu P'^*_{b\beta} \partial_\alpha \mathbb{P}_{ab}, \quad (7)$$

$$\mathcal{L}_{P^*P^*\mathbb{V}} = i\frac{\beta g_V}{\sqrt{2}} P^{*\dagger}_{a\nu} \overleftrightarrow{\partial}_\mu P^{*\nu}_b \mathbb{V}^\mu_{ba} + i2\sqrt{2}\lambda g_V M^* P^{*\dagger}_{a\mu} P^*_{b\nu} \mathbb{V}^{\mu\nu}_{ba} - i\frac{\beta g_V}{\sqrt{2}} P'^{*\dagger}_{a\nu} \overleftrightarrow{\partial}_\mu P'^{*\nu}_b \mathbb{V}^\mu_{ab} - i2\sqrt{2}\lambda g_V M^* P'^{*\dagger}_{a\mu} P'^*_{b\nu} \mathbb{V}^{\mu\nu}_{ab}, \quad (8)$$

$$\mathcal{L}_{P^*P^*\sigma} = 2g_\sigma M^* P^{*\dagger}_{a\mu} \sigma P^{*\mu}_a + 2g_\sigma M^* P'^{*\dagger}_{a\mu} \sigma P'^{*\mu}_a, \quad (9)$$

$$\mathcal{L}_{P^*P\mathbb{P}} = -\frac{2g}{f_\pi}\sqrt{MM^*}(P_a^\dagger P^*_{b\mu} + P^{*\dagger}_{a\mu} P_b)\partial^\mu \mathbb{P}_{ba} + \frac{2g}{f_\pi}\sqrt{MM^*}(P'^\dagger_a P'^*_{b\mu} + P'^{*\dagger}_{a\mu} P'_b)\partial^\mu \mathbb{P}_{ab}, \quad (10)$$

$$\mathcal{L}_{P^*P\mathbb{V}} = -i\sqrt{2}\lambda g_V \epsilon^{\beta\alpha\mu\nu}(P_a^\dagger \overleftrightarrow{\partial}_\beta P^*_{b\alpha} + P^{*\dagger}_{a\alpha} \overleftrightarrow{\partial}_\beta P_b)(\partial_\mu \mathbb{V}_\nu)_{ba} - i\sqrt{2}\lambda g_V \epsilon^{\beta\alpha\mu\nu}(P'^\dagger_a \overleftrightarrow{\partial}_\beta P'^*_{b\alpha} + P'^{*\dagger}_{a\alpha} \overleftrightarrow{\partial}_\beta P'_b)(\partial_\mu \mathbb{V}_\nu)_{ab}, \quad (11)$$

where $\overleftrightarrow{\partial} = \overrightarrow{\partial} - \overleftarrow{\partial}$. The symbol σ represents the lowest isoscalar-scalar meson. The matrices for heavy mesons and antiheavy mesons $P^{(*)}$ and $P'^{(*)}$ are defined as

$$P = (D^0, D^+, D_s^+), \qquad P^*_\mu = (D^{*0}_\mu, D^{*+}_\mu, D^{*+}_{s\mu}), \qquad P' = (\bar{D}^0, D^-, D_s^-), \qquad P'^*_\mu = (\bar{D}^{*0}_\mu, D^{*-}_\mu, D^{*-}_{s\mu}), \quad (12)$$

while the matrices for light pseudoscalar and vector mesons are expressed as

$$\mathbb{P} = \begin{pmatrix} \frac{1}{\sqrt{2}}\pi^0 + \frac{1}{\sqrt{6}}\eta & \pi^+ & K^+ \\ \pi^- & -\frac{1}{\sqrt{2}}\pi^0 + \frac{1}{\sqrt{6}}\eta & K^0 \\ K^- & \bar{K}^0 & -\frac{2}{\sqrt{6}}\eta \end{pmatrix}, \qquad \mathbb{V}_\mu = \begin{pmatrix} \frac{1}{\sqrt{2}}\rho^0_\mu + \frac{1}{\sqrt{2}}\omega_\mu & \rho^+_\mu & K^{*+}_\mu \\ \rho^-_\mu & -\frac{1}{\sqrt{2}}\rho^0_\mu + \frac{1}{\sqrt{2}}\omega_\mu & K^{*0}_\mu \\ K^{*-}_\mu & \bar{K}^{*0}_\mu & \phi_\mu \end{pmatrix}. \quad (13)$$

The coupling constants in the Lagrangian are taken from Ref. [26]: $g = 0.59 \pm 0.07 \pm 0.01$, determined from experimental measurements of the full width of the D^{*+}; $g_V = m_\rho/f_\pi \approx 5.8$, obtained via the Kawarabayashi-Suzuki-Riazuddin-Fayyazuddin relation with $f_\pi = 132$ MeV; $\beta \approx 0.9$ [27,28], based on the vector meson dominance in the radiative decay of heavy mesons; and $\lambda = -0.56$ GeV^{-1}, derived from light-cone sum rules and lattice QCD results. It should be noted that we adopt a different sign convention for λ compared to Ref. [26], as we use the same phase for heavy vector mesons as in Ref. [25]. The coupling constant for the sigma meson is used to evaluate the 2π transition of $D_s(1^+)$ in Ref. [29]. The coupling for the lowest isoscalar-scalar meson is given by $g_\sigma = \frac{g_\pi}{2\sqrt{6}}$ with $g_\pi = 3.73$.

Regarding the effective Lagrangian for the heavy baryon, we adopt it from Ref. [30], which considers a more comprehensive form of the Lagrangian as discussed in Ref. [31]. The baryonic interaction vertices in the tree-level meson-exchange diagrams are characterized by the following effective Lagrangian:

$$\mathcal{L}_{B_{\bar{3}}B_{\bar{3}}\mathbb{V}} = \frac{i\beta_{\bar{3}} g_V}{2\sqrt{2}M_{\bar{3}}}(\bar{B}_{\bar{3}} \overleftrightarrow{\partial}_\mu \mathbb{V}^\mu B_{\bar{3}}), \quad (14)$$

$$\mathcal{L}_{B_{\bar{3}}B_{\bar{3}}\sigma} = l_{\bar{3}}(\bar{B}_{\bar{3}}\sigma B_{\bar{3}}), \quad (15)$$

$$\mathcal{L}_{B_6B_6\mathbb{P}} = i\frac{g_1}{2f_\pi M_6}\bar{B}_6\gamma_5(\gamma^\alpha\gamma^\beta - g^{\alpha\beta})\overleftrightarrow{\partial}_\alpha\partial_\beta \mathbb{P} B_6, \quad (16)$$

$$\mathcal{L}_{B_6B_6\mathbb{V}} = -i\frac{\beta_6 g_V}{2\sqrt{2}M_6}(\bar{B}_6 \overleftrightarrow{\partial}_\alpha \mathbb{V}^\alpha B_6) - \frac{i\lambda_6 g_V}{3\sqrt{2}}(\bar{B}_6\gamma_\mu\gamma_\nu \mathbb{V}^{\mu\nu} B_6), \quad (17)$$

$$\mathcal{L}_{B_6B_6\sigma} = -l_6(\bar{B}_6\sigma B_6), \tag{18}$$

$$\mathcal{L}_{B_6^*B_6^*\mathbb{P}} = \frac{3g_1}{4f_\pi M_6^*}\epsilon^{\mu\nu\alpha\beta}(\bar{B}_{6\mu}^* \overleftrightarrow{\partial}_\nu \partial_\alpha \mathbb{P} B_{6\beta}^*), \tag{19}$$

$$\mathcal{L}_{B_6^*B_6^*\mathbb{V}} = i\frac{\beta_6 g_V}{2\sqrt{2}M_6^*}(\bar{B}_{6\mu}^* \overleftrightarrow{\partial}_\alpha \mathbb{V}^\alpha B_6^{*\mu}) + \frac{i\lambda_6 g_V}{\sqrt{2}}(\bar{B}_{6\mu}^* \mathbb{V}^{\mu\nu} B_{6\nu}^*), \tag{20}$$

$$\mathcal{L}_{B_6^*B_6^*\sigma} = l_6(\bar{B}_{6\mu}^* \sigma B_6^{*\mu}), \tag{21}$$

$$\mathcal{L}_{B_6B_6^*\mathbb{P}} = \frac{g_1}{4f_\pi}\sqrt{\frac{3}{M_6^* M_6}}\epsilon^{\mu\nu\alpha\beta}[(\bar{B}_6\gamma_5\gamma_\mu \overleftrightarrow{\partial}_\nu \partial_\alpha \mathbb{P} B_{6\beta}^*) + (\bar{B}_{6\mu}^*\gamma_5\gamma_\nu \overleftrightarrow{\partial}_\alpha \partial_\beta \mathbb{P} B_6)], \tag{22}$$

$$\mathcal{L}_{B_6B_6^*\mathbb{V}} = \frac{i\lambda_6 g_V}{\sqrt{6}}\left[\bar{B}_6\gamma_5\left(\gamma_\mu + \frac{i\overleftrightarrow{\partial}_\mu}{2\sqrt{M_6^* M_6}}\right)\mathbb{V}^{\mu\nu}B_{6\nu}^* + \bar{B}_{6\mu}^*\gamma_5\left(\gamma_\nu - \frac{i\overleftrightarrow{\partial}_\nu}{2\sqrt{M_6^* M_6}}\right)\mathbb{V}^{\mu\nu}B_6\right], \tag{23}$$

$$\mathcal{L}_{B_6B_{\bar{3}}\mathbb{P}} = -\frac{g_4}{\sqrt{3}f_\pi}\left[\bar{B}_6\gamma_5\left(\gamma_\mu + \frac{i\overleftrightarrow{\partial}_\mu}{2\sqrt{M_6 M_{\bar{3}}}}\right)\partial^\mu \mathbb{P} B_{\bar{3}} + \bar{B}_{\bar{3}}\gamma_5\left(\gamma_\mu - \frac{i\overleftrightarrow{\partial}_\mu}{2\sqrt{M_6 M_{\bar{3}}}}\right)\partial^\mu \mathbb{P} B_6\right], \tag{24}$$

$$\mathcal{L}_{B_6B_{\bar{3}}\mathbb{V}} = i\frac{\lambda_{6\bar{3}} g_V}{\sqrt{6M_6 M_{\bar{3}}}}\epsilon^{\mu\nu\alpha\beta}[(\bar{B}_6\gamma_5\gamma_\mu \overleftrightarrow{\partial}_\nu \partial_\alpha \mathbb{V}_\beta B_{\bar{3}}) + (\bar{B}_{\bar{3}}\gamma_5\gamma_\mu \overleftrightarrow{\partial}_\nu \partial_\alpha \mathbb{V}_\beta B_6)], \tag{25}$$

$$\mathcal{L}_{B_6^*B_{\bar{3}}\mathbb{P}} = -\frac{g_4}{f_\pi}[(\bar{B}_{6\mu}^* \partial^\mu \mathbb{P} B_{\bar{3}}) + (\bar{B}_{\bar{3}}\partial^\mu \mathbb{P} B_{6\mu}^*)], \tag{26}$$

$$\mathcal{L}_{B_6^*B_{\bar{3}}\mathbb{V}} = i\frac{\lambda_{6\bar{3}} g_V}{\sqrt{2M_6^* M_{\bar{3}}}}\epsilon^{\mu\nu\alpha\beta}[(\bar{B}_{6\mu}^* \overleftrightarrow{\partial}_\nu \partial_\alpha \mathbb{V}_\beta B_{\bar{3}}) + (\bar{B}_{\bar{3}} \overleftrightarrow{\partial}_\nu \partial_\alpha \mathbb{V}_\beta B_{6\mu}^*)], \tag{27}$$

where the heavy baryon fields are expressed as

$$B_{\bar{3}} = \begin{pmatrix} 0 & \Lambda_c^+ & \Xi_c^+ \\ -\Lambda_c^+ & 0 & \Xi_c^0 \\ -\Xi_c^+ & -\Xi_c^0 & 0 \end{pmatrix}, \quad B_6 = \begin{pmatrix} \Sigma_c^{++} & \frac{1}{\sqrt{2}}\Sigma_c^+ & \frac{1}{\sqrt{2}}\Xi_c'^+ \\ \frac{1}{\sqrt{2}}\Sigma_c^+ & \Sigma_c^0 & \frac{1}{\sqrt{2}}\Xi_c'^0 \\ \frac{1}{\sqrt{2}}\Xi_c'^+ & \frac{1}{\sqrt{2}}\Xi_c'^0 & \Omega_c^0 \end{pmatrix}, \quad B_6^* = \begin{pmatrix} \Sigma_c^{*++} & \frac{1}{\sqrt{2}}\Sigma_c^{*+} & \frac{1}{\sqrt{2}}\Xi_c^{*+} \\ \frac{1}{\sqrt{2}}\Sigma_c^{*+} & \Sigma_c^{*0} & \frac{1}{\sqrt{2}}\Xi_c^{*0} \\ \frac{1}{\sqrt{2}}\Xi_c^{*+} & \frac{1}{\sqrt{2}}\Xi_c^{*0} & \Omega_c^{*0} \end{pmatrix}. \tag{28}$$

Here, B_μ represents the spin $3/2$ Rarita-Schwinger field, which must satisfy the following constraints:

$$p^\mu B_\mu = 0 \quad \text{and} \quad \gamma^\mu B_\mu = 0. \tag{29}$$

The coupling constants within the effective Lagrangian are specified as follows [30,32]: $\beta_{\bar{3}} = 6/g_V$, $\beta_6 = -2\beta_{\bar{3}}$, $\lambda_6 = -3.31\ \text{GeV}^{-1}$, $\lambda_{6\bar{3}} = -\lambda_6/\sqrt{8}$, $g_1 = 0.942$, $g_4 = 0.999$, $l_{\bar{3}} = -3.1$, and $l_6 = -2l_{\bar{3}}$. The sign conventions employed here are consistent with those in Refs. [32,33].

For the inclusion of hidden-charm channels, we require an effective Lagrangian that describes the coupling between heavy mesons and quarkonium. We utilize the Lagrangian from Ref. [34], given by

$$\mathcal{L}_{PPJ/\psi} = -ig_\psi M\sqrt{m_J}(J/\psi^\mu P^\dagger \overleftrightarrow{\partial}_\mu P\prime^\dagger) + \text{H.c.}, \tag{30}$$

$$\mathcal{L}_{P^*PJ/\psi} = ig_\psi\sqrt{\frac{MM^*}{m_J}}\epsilon^{\mu\nu\alpha\beta}\partial_\mu J/\psi_\nu(P^\dagger \overleftrightarrow{\partial}_\alpha P^*\prime_\beta^\dagger + P_\beta^{*\dagger} \overleftrightarrow{\partial}_\alpha P\prime^\dagger) + \text{H.c.}, \tag{31}$$

$$\mathcal{L}_{P^*P^*J/\psi} = ig_\psi M^*\sqrt{m_J}(g^{\mu\nu}g^{\alpha\beta} - g^{\mu\alpha}g^{\nu\beta} + g^{\mu\beta}g^{\nu\alpha})(J/\psi_\mu P_\nu^{*\dagger} \overleftrightarrow{\partial}_\alpha P^*\prime_\beta^\dagger) + \text{H.c.} \tag{32}$$

In the present study, we focus exclusively on vector quarkonia due to their direct experimental relevance. Nevertheless, extending the analysis to include pseudoscalar states is straightforward, as we apply heavy-quark spin symmetry to the quarkonium sector as well [35]. In the absence of experimental data for the $J/\psi \to D\bar{D}$ decay, Shimizu and Harada [36] provided an estimate for the coupling constant g_ψ using the following approach: they first determined the coupling constant $g_{\phi K\bar{K}}$ from the experimental decay width of $\phi \to K\bar{K}$. Assuming that the decay mechanisms of the J/ψ are analogous to those of the ϕ, aside from mass differences, they estimated the coupling constant as $g_\psi = 0.679\ \mathrm{GeV}^{-3/2}$. The coupling constants between heavy baryons and heavy mesons are formulated following Ref. [36]:

$$\mathcal{L}_{B_8B_3P} = -g_{I\bar{3}}\sqrt{M}\bar{B}_{\bar{3}}\gamma_5 PN + \mathrm{H.c.}, \tag{33}$$

$$\mathcal{L}_{B_8B_3P^*} = g_{I\bar{3}}\sqrt{M^*}\bar{B}_{\bar{3}}\gamma^\mu P^*_\mu N + \mathrm{H.c.}, \tag{34}$$

$$\mathcal{L}_{B_8B_6P} = g_{I6}\sqrt{3M}\bar{B}_6\gamma_5 B_8 P + \mathrm{H.c.}, \tag{35}$$

$$\mathcal{L}_{B_8B_6P^*} = g_{I6}\sqrt{\frac{M^*}{3}}\bar{B}_6\gamma^\nu B_8 P^*_\nu + \mathrm{H.c.}, \tag{36}$$

$$\mathcal{L}_{B_8B_6^*P^*} = 2g_{I6}\sqrt{M^*}\bar{B}^\mu_6\gamma_5 B_8 P^*_\mu + \mathrm{H.c.}. \tag{37}$$

We adopt the coupling constants $g_{I\bar{3}} = -9.88\ \mathrm{GeV}^{-1/2}$ and $g_{I6} = 1.14\ \mathrm{GeV}^{-1/2}$ from Ref. [36]. It should be emphasized that the coupling to hidden-charm channels has only a minimal impact on the resonance production mechanism. The calculations indicate that, although these coupling constants are based on approximate estimates, the predicted masses of the hidden-charm pentaquarks remain largely unchanged. This finding suggests that the $J/\psi\Lambda$ channel contributes only marginally to the formation of heavy pentaquarks.

The Feynman amplitude for a one-meson exchange diagram can be expressed as

$$\mathcal{A}_{\lambda_1'\lambda_2',\lambda_1\lambda_2} = \mathrm{IS}F^2(q^2)\Gamma_{\lambda_1'\lambda_2'}(p_1', p_2')\mathcal{P}(q)\Gamma_{\lambda_1\lambda_2}(p_1, p_2), \tag{38}$$

where λ_i and p_i represent the helicity and momentum of the corresponding particle, and q is the momentum of the exchanged particle. The IS factor corresponds to the SU(3) Clebsch-Gordan coefficient and isospin factor, and is tabulated in Table I for each exchange diagram. The vertex Γ is obtained from the effective Lagrangian previously described, and the propagators for the spin-0 and spin-1 mesons are given by

$$\mathcal{P}(q) = \frac{1}{q^2 - m^2}, \qquad \mathcal{P}_{\mu\nu}(q) = \frac{1}{q^2 - m^2}\left(-g_{\mu\nu} + \frac{q_\mu q_\nu}{m^2}\right). \tag{39}$$

For simplicity, we employ the static propagator for pion exchange, given by $\mathcal{P}_\pi(q) = -1/(\boldsymbol{q}^2 + m_\pi^2)$. For the heavy-meson propagators, we adopt the same form as for light mesons, since the heavy-quark mass is finite. Furthermore, parity invariance reduces the number of contributing processes. The parity relation is expressed as

$$\mathcal{A}_{-\lambda_1'-\lambda_2',-\lambda_1-\lambda_2} = \eta(\eta')^{-1}\mathcal{A}_{\lambda_1'\lambda_2',\lambda_1\lambda_2}, \tag{40}$$

where η and η' are defined as

$$\eta = \eta_1\eta_2(-1)^{J-s_1-s_2}, \qquad \eta' = \eta_1'\eta_2'(-1)^{J-s_1'-s_2'}. \tag{41}$$

Here, η_i and s_i designate, respectively, the intrinsic parity and spin of the particle, and J denotes the total angular momentum.

To account for the finite size of hadrons, we introduce a form factor at each vertex. We adopt the following parametrization [37]:

$$F(q^2) = \left(\frac{n\Lambda^2 - m^2}{n\Lambda^2 - q^2}\right)^n, \tag{42}$$

where n is determined by the momentum power in the vertex. This parametrization has the advantage that adjusting Λ is not necessary when varying n. It is noteworthy that, in the limit $n \to \infty$, Eq. (42) reduces to a Gaussian form. Although the cutoff masses Λ in Eq. (42) are not experimentally determined for heavy-hadron processes, we implement a strategy to minimize the associated uncertainties. Recent studies have shown that heavy hadrons possess more compact structures than their light counterparts [38,39], suggesting that the cutoff masses for heavy hadrons should be larger than those for light hadrons. Accordingly, we define the cutoff mass as $\Lambda = \Lambda_0 + m$, where m denotes the mass of the exchanged meson. We choose Λ_0 values in the range of approximately 500–700 MeV for each channel, as summarized in Table I, allowing for a minimal fitting procedure.

To simplify the numerical calculations and clarify the spin-parity assignments for $P_{c\bar{c}s}$ states, we perform a partial-wave expansion of the $\mathcal{V}$ and $\mathcal{T}$ matrices. This results in a one-dimensional integral equation,

$$\mathcal{T}^{J(fi)}_{\lambda'\lambda}(\mathrm{p}', \mathrm{p}) = \mathcal{V}^{J(fi)}_{\lambda'\lambda}(\mathrm{p}', \mathrm{p}) + \frac{1}{(2\pi)^3}\sum_{k,\lambda_k}\int \frac{\mathrm{q}^2 d\mathrm{q}}{2E_{k1}E_{k2}}\mathcal{V}^{J(fk)}_{\lambda'\lambda_k}(\mathrm{p}', \mathrm{q})\frac{E_k}{s - E_k^2 + i\varepsilon}\mathcal{T}^{J(ki)}_{\lambda_k\lambda}(\mathrm{q}, \mathrm{p}), \tag{43}$$

TABLE I. Values of the IS factors and $\Lambda - m$ for the corresponding t-channel diagrams for the given reactions. Λ denotes the cutoff mass and m stands for the mass of the exchanged particle, given in units of MeV.

Reactions	Exchange particles	IS	$\Lambda - m$
$J/\psi\Lambda \to \bar{D}_s\Lambda_c$	$\bar{D}_s$, $\bar{D}_s^*$	$-\frac{1}{3}\sqrt{6}$	600
$J/\psi\Lambda \to \bar{D}\Xi_c$	$\bar{D}$, $\bar{D}^*$	$-\frac{1}{3}\sqrt{3}$	600
$J/\psi\Lambda \to \bar{D}_s^*\Lambda_c$	$\bar{D}_s$, $\bar{D}_s^*$	$-\frac{1}{3}\sqrt{6}$	600
$J/\psi\Lambda \to \bar{D}\Xi_c'$	$\bar{D}$, $\bar{D}^*$	$\frac{1}{2}\sqrt{6}$	600
$J/\psi\Lambda \to \bar{D}^*\Xi_c$	$\bar{D}$, $\bar{D}^*$	$-\frac{1}{3}\sqrt{3}$	600
$J/\psi\Lambda \to \bar{D}\Xi_c^*$	$\bar{D}$, $\bar{D}^*$	$\frac{1}{2}\sqrt{6}$	600
$J/\psi\Lambda \to \bar{D}^*\Xi_c'$	$\bar{D}$, $\bar{D}^*$	$\frac{1}{2}\sqrt{6}$	600
$J/\psi\Lambda \to \bar{D}^*\Xi_c^*$	$\bar{D}$, $\bar{D}^*$	$\frac{1}{2}\sqrt{6}$	600
$\bar{D}_s\Lambda_c \to \bar{D}_s\Lambda_c$	σ	2	600
$\bar{D}_s\Lambda_c \to \bar{D}\Xi_c$	K^*	$\sqrt{2}$	600
$\bar{D}_s\Lambda_c \to \bar{D}\Xi_c'$	K^*	-1	600
$\bar{D}_s\Lambda_c \to \bar{D}^*\Xi_c$	K^*	$\sqrt{2}$	600
$\bar{D}_s\Lambda_c \to \bar{D}\Xi_c^*$	K^*	-1	600
$\bar{D}_s\Lambda_c \to \bar{D}^*\Xi_c'$	K, K^*	-1	600
$\bar{D}_s\Lambda_c \to \bar{D}^*\Xi_c^*$	K, K^*	-1	600
$\bar{D}\Xi_c \to \bar{D}\Xi_c$	ρ	$-\frac{3}{2}$	600
	ω	$\frac{1}{2}$	600
	σ	2	600
$\bar{D}\Xi_c \to \bar{D}_s^*\Lambda_c$	K^*	$\sqrt{2}$	600
$\bar{D}\Xi_c \to \bar{D}\Xi_c'$	ρ	$-\frac{3}{4}\sqrt{2}$	600
	ω	$\frac{1}{4}\sqrt{2}$	600
$\bar{D}\Xi_c \to \bar{D}^*\Xi_c$	ρ	$-\frac{3}{2}$	600
	ω	$\frac{1}{2}$	600
$\bar{D}\Xi_c \to \bar{D}\Xi_c^*$	ρ	$-\frac{3}{4}\sqrt{2}$	600
	ω	$\frac{1}{4}\sqrt{2}$	600
$\bar{D}\Xi_c \to \bar{D}^*\Xi_c'$	π	$-\frac{3}{4}\sqrt{2}$	600
	η	$\frac{1}{4}\sqrt{2}$	600
	ρ	$-\frac{3}{4}\sqrt{2}$	600
	ω	$\frac{1}{4}\sqrt{2}$	600
$\bar{D}\Xi_c \to \bar{D}^*\Xi_c^*$	π	$-\frac{3}{4}\sqrt{2}$	600
	η	$\frac{1}{4}\sqrt{2}$	600
	ρ	$-\frac{3}{4}\sqrt{2}$	600
	ω	$\frac{1}{4}\sqrt{2}$	600
$\bar{D}_s^*\Lambda_c \to \bar{D}_s^*\Lambda_c$	σ	2	600
$\bar{D}_s^*\Lambda_c \to \bar{D}\Xi_c'$	K, K^*	-1	600
$\bar{D}_s^*\Lambda_c \to \bar{D}^*\Xi_c$	K^*	$\sqrt{2}$	600
$\bar{D}_s^*\Lambda_c \to \bar{D}\Xi_c^*$	K, K^*	-1	600
$\bar{D}_s^*\Lambda_c \to \bar{D}^*\Xi_c'$	K, K^*	-1	600
$\bar{D}_s^*\Lambda_c \to \bar{D}^*\Xi_c^*$	K, K^*	-1	600
$\bar{D}\Xi_c' \to \bar{D}\Xi_c'$	ρ	$-\frac{3}{4}$	600
	ω	$\frac{1}{4}$	600
	σ	1	600
$\bar{D}\Xi_c' \to \bar{D}^*\Xi_c$	π	$-\frac{3}{4}\sqrt{2}$	600
	η	$\frac{1}{4}\sqrt{2}$	600
	ρ	$-\frac{3}{4}\sqrt{2}$	600
	ω	$\frac{1}{4}\sqrt{2}$	600
$\bar{D}\Xi_c' \to \bar{D}\Xi_c^*$	ρ	$-\frac{3}{4}$	600
	ω	$\frac{1}{4}$	600
$\bar{D}\Xi_c' \to \bar{D}^*\Xi_c^*$	π	$-\frac{3}{4}$	600
	η	$-\frac{1}{12}$	600
	ρ	$-\frac{3}{4}$	600
	ω	$\frac{1}{4}$	600
$\bar{D}^*\Xi_c \to \bar{D}^*\Xi_c$	ρ	$-\frac{3}{2}$	600
	ω	$\frac{1}{2}$	600
	σ	2	600
$\bar{D}^*\Xi_c \to \bar{D}\Xi_c^*$	π	$-\frac{3}{4}\sqrt{2}$	600
	η	$\frac{1}{4}\sqrt{2}$	600
	ρ	$-\frac{3}{4}\sqrt{2}$	600
	ω	$\frac{1}{4}\sqrt{2}$	600
$\bar{D}^*\Xi_c \to \bar{D}^*\Xi_c'$	π	$-\frac{3}{4}\sqrt{2}$	600
	η	$\frac{1}{4}\sqrt{2}$	600
	ρ	$-\frac{3}{4}\sqrt{2}$	600
	ω	$\frac{1}{4}\sqrt{2}$	600
$\bar{D}^*\Xi_c \to \bar{D}^*\Xi_c^*$	π	$-\frac{3}{4}\sqrt{2}$	600
	η	$\frac{1}{4}\sqrt{2}$	600
	ρ	$-\frac{3}{4}\sqrt{2}$	600
	ω	$\frac{1}{4}\sqrt{2}$	600
$\bar{D}\Xi_c^* \to \bar{D}\Xi_c^*$	ρ	$-\frac{3}{4}$	700
	ω	$\frac{1}{4}$	700
	σ	1	700
$\bar{D}\Xi_c^* \to \bar{D}^*\Xi_c'$	π	$-\frac{3}{4}$	700
	η	$-\frac{1}{12}$	700
	ρ	$-\frac{3}{4}$	700
	ω	$\frac{1}{4}$	700
$\bar{D}\Xi_c^* \to \bar{D}^*\Xi_c^*$	π	$-\frac{3}{4}$	700
	η	$-\frac{1}{12}$	700
	ρ	$-\frac{3}{4}$	700
	ω	$\frac{1}{4}$	700
$\bar{D}^*\Xi_c' \to \bar{D}^*\Xi_c'$	π	$-\frac{3}{4}$	700
	η	$-\frac{1}{12}$	700
	ρ	$-\frac{3}{4}$	700
	ω	$\frac{1}{4}$	700
	σ	1	700
$\bar{D}^*\Xi_c' \to \bar{D}^*\Xi_c^*$	π	$-\frac{3}{4}$	700
	η	$-\frac{1}{12}$	700
	ρ	$-\frac{3}{4}$	700
	ω	$\frac{1}{4}$	700
$\bar{D}^*\Xi_c^* \to \bar{D}^*\Xi_c^*$	π	$-\frac{3}{4}$	700
	η	$-\frac{1}{12}$	700

(Table continued)

TABLE I. *(Continued)*

Reactions	Exchange particles	IS	$\Lambda - m$
	ρ	$-\frac{3}{4}$	700
	ω	$\frac{1}{4}$	700
	σ	1	700

where $\lambda' = \{\lambda_1', \lambda_2'\}$, $\lambda = \{\lambda_1, \lambda_2\}$, and $\lambda_k = \{\lambda_{k1}, \lambda_{k2}\}$ denote the helicities of the final (f), initial (i), and intermediate (k) states. The variables p′, p, and q represent the magnitudes of momentum vectors $\boldsymbol{p}'$, $\boldsymbol{p}$, and $\boldsymbol{q}$, respectively.

The partial-wave kernel amplitudes $\mathcal{V}^{J(fi)}_{\lambda'\lambda}$ are formulated as

$$\mathcal{V}^{J(fi)}_{\lambda'\lambda}(\mathrm{p}', \mathrm{p}) = 2\pi \int d(\cos\theta) d^J_{\lambda_1-\lambda_2,\lambda_1'-\lambda_2'}(\theta) \mathcal{V}^{fi}_{\lambda'\lambda}(\mathrm{p}', \mathrm{p}, \theta), \tag{44}$$

where θ is the scattering angle and $d^J_{\lambda_f\lambda_i}(\theta)$ represents the reduced Wigner D functions.

The integral equation in Eq. (43) contains a singularity arising from the two-body propagator $\mathcal{G}$. To handle this singularity, we isolate and treat its singular component separately. The regularized integral equation is written as

$$\mathcal{T}^{fi}_{\lambda'\lambda}(\mathrm{p}', \mathrm{p}) = \mathcal{V}^{fi}_{\lambda'\lambda}(\mathrm{p}', \mathrm{p}) + \frac{1}{(2\pi)^3} \sum_{k,\lambda_k} \left[\int_0^\infty d\mathrm{q} \frac{\mathrm{q} E_k}{E_{k1} E_{k2}} \frac{\mathcal{F}(\mathrm{q}) - \mathcal{F}(\tilde{\mathrm{q}}_k)}{s - E_k^2} + \frac{1}{2\sqrt{s}} \left(\ln \left| \frac{\sqrt{s} - E_k^{\mathrm{thr}}}{\sqrt{s} + E_k^{\mathrm{thr}}} \right| - i\pi \right) \mathcal{F}(\tilde{\mathrm{q}}_k) \right], \tag{45}$$

with

$$\mathcal{F}(\mathrm{q}) = \frac{1}{2} \mathrm{q} \mathcal{V}^{fk}_{\lambda'\lambda_k}(\mathrm{p}', \mathrm{q}) \mathcal{T}^{ki}_{\lambda_k\lambda}(\mathrm{q}, \mathrm{p}), \tag{46}$$

and $\tilde{\mathrm{q}}_k$ denotes the momentum q when $E_{k1} + E_{k2} = \sqrt{s}$. Regularization is applied only when the total energy $\sqrt{s}$ exceeds the threshold energy of the kth channel E_k^{thr}. It is worth noting that the form factors in the kernel amplitudes $\mathcal{V}$ ensure the unitarity of the transition amplitudes in the high-momentum region.

To compute the $\mathcal{T}$ matrix numerically in Eq. (45), we expand the $\mathcal{V}$ matrix in the helicity basis and express it in momentum space, where the momenta are determined using the Gaussian quadrature method. The $\mathcal{T}$ matrix is then obtained by applying the Haftel-Tabakin matrix inversion method [40]

$$\mathcal{T} = (1 - \mathcal{V}\tilde{\mathcal{G}})^{-1} \mathcal{V}. \tag{47}$$

The resulting $\mathcal{T}$ matrix is expressed in the helicity basis and does not possess definite parity. To analyze the parity assignments of the $P_{c\bar{c}s}$ states, we decompose the transition amplitudes into partial-wave amplitudes with definite parity, as follows:

$$\mathcal{T}^{J\pm}_{\lambda'\lambda} = \frac{1}{2} [\mathcal{T}^J_{\lambda'\lambda} \pm \eta_1\eta_2(-1)^{s_1+s_2+\frac{1}{2}} \mathcal{T}^J_{\lambda'-\lambda}], \tag{48}$$

where $\mathcal{T}^{J\pm}$ denotes the partial-wave transition amplitude with total angular momentum J and parity $(-1)^{J\pm 1/2}$. The factor $1/2$ ensures that no additional factor is needed when transforming back to the partial-wave component:

$$\mathcal{T}^J_{\lambda'\lambda} = \mathcal{T}^{J+}_{\lambda'\lambda} + \mathcal{T}^{J-}_{\lambda'\lambda}. \tag{49}$$

We emphasize that it is unnecessary to decompose the partial-wave component with definite parity in Eq. (43), as parity invariance is already incorporated in both the effective Lagrangian and the amplitude calculations, as shown in Eq. (40). To investigate the dynamical generation of resonances, we express the $\mathcal{T}$ matrix in the IJL particle basis [41]. The relations between the $\mathcal{T}$ matrix elements in the two bases are given by

$$\begin{aligned} \mathcal{T}^{JS'S}_{L'L} = & \frac{\sqrt{(2L+1)(2L'+1)}}{2J+1} \\ & \times \sum_{\lambda_1'\lambda_2'\lambda_1\lambda_2} (L'0S'\lambda'|J\lambda')(s_1'\lambda_1's_2' - \lambda_2'|S'\lambda') \\ & \times (L0S\lambda|J\lambda)(s_1\lambda_1 s_2 - \lambda_2|S\lambda) \mathcal{T}^J_{\lambda_1'\lambda_2',\lambda_1\lambda_2}. \end{aligned} \tag{50}$$

In this work, we present only the diagonal part $\mathcal{T}^{JS}_L$, as it is most relevant to particle production.

III. RESULTS AND DISCUSSIONS

The singly strange hidden-charm pentaquark was first observed by the LHCb Collaboration in the decay $\Xi_b^- \to J/\psi\Lambda K^-$ [42]. The collaboration identified a hidden-charm pentaquark state with strangeness $S = -1$, denoted as $P_{c\bar{c}s}(4459)$. However, due to limited data, one could not rule out the possibility that the observed signal originated from two distinct states. We find a narrow peak structure around 4.40 GeV, accompanied by a slightly broader feature nearby. Based on these results, it is anticipated that additional $P_{c\bar{c}s}$ candidates will be discovered by measuring the $\Xi_b^- \to J/\psi\Lambda K^-$ more precisely. Very recently, the Belle Collaboration confirmed the existence of $P_{c\bar{c}s}(4459)$ MeV [5] with a slightly larger mass.

Two years later, the LHCb Collaboration reported the discovery of a new $P_{c\bar{c}s}$ state in a different decay mode, specifically $B^- \to J/\psi\Lambda\bar{p}$ [4]. It is located at around 4.34 GeV, just below the $\bar{D}\Xi_c$ threshold. The spin-paritty

of the newly observed state was assigned to be $J^P = 1/2^-$, making it the first hidden-charm pentaquark with an experimentally established spin-parity. Numerous studies have suggested that $P_{c\bar{c}s}(4338)$ is associated with a molecular $\bar{D}\Xi_c$ state with $J^P = 1/2^-$ [12–14,16]. Additionally, LHCb investigated the possibility of a narrow resonance near the $\bar{D}_s\Lambda_c$ threshold; however, this signal was not found to be statistically significant.

In this section, we will show how the $P_{c\bar{c}s}$ states are generated dynamically by using the present formalism. We then discuss the nature of these singly strange hidden-charm pentaquarks. We restrict our discussion to the case of zero total isospin, since we only consider the $P_{c\bar{c}s}$ production in the $J/\psi\Lambda$ final state. In Table I, we present the IS factors and cutoff masses for each exchange in the respective channels. As in the case of the nonstrange hidden-charm pentaquarks, we employ smaller cutoff mass values for transitions to lower channels ($J/\psi\Lambda$, $\bar{D}_s\Lambda_c$, $\bar{D}\Xi_c$, $\bar{D}_s^*\Lambda_c$, $\bar{D}\Xi_c'$, and $\bar{D}^*\Xi_c$). This adjustment is necessary to reproduce the experimentally observed hidden-charm pentaquark states $P_{c\bar{c}s}(4338)$ and $P_{c\bar{c}s}(4459)$ with $S = -1$.

A. Negative parity states

We begin by discussing the numerical results for the $P_{c\bar{c}s}$ states with negative parity. As previously mentioned, while $P_{c\bar{c}s}(4338)$ most likely has $J^P = 1/2^-$, the spin-parity assignment of $P_{c\bar{c}s}(4459)$ remains uncertain. In the present work, the results suggest that $P_{c\bar{c}s}(4459)$ has negative parity as well.

Figure 4 displays the partial-wave cross sections for the transitions of various initial states with $S = -1$ to the $J/\psi\Lambda$ final state as functions of the $J/\psi\Lambda$ invariant mass. In the $J^P = 1/2^-$ channel shown in the upper left panel of Fig. 4, we identify four peaks: a narrow peak below the $\bar{D}\Xi_c$ threshold, two peaks below the $\bar{D}\Xi_c'$ threshold, and a broad peak below the $\bar{D}^*\Xi_c'$ threshold. While the first peak can be associated with the known $P_{c\bar{c}s}(4338)$, the remaining peaks have not yet been discovered experimentally. However, given the large cross sections of the two peaks below the $\bar{D}\Xi_c'$ threshold, their experimental observation seems probable. Examining the LHCb data for the decay of $\Xi_b^- \to J/\psi\Lambda\bar{p}$ [42], there are indications of possible structures around 4.4 GeV in the $J/\psi\Lambda$ invariant mass spectrum,

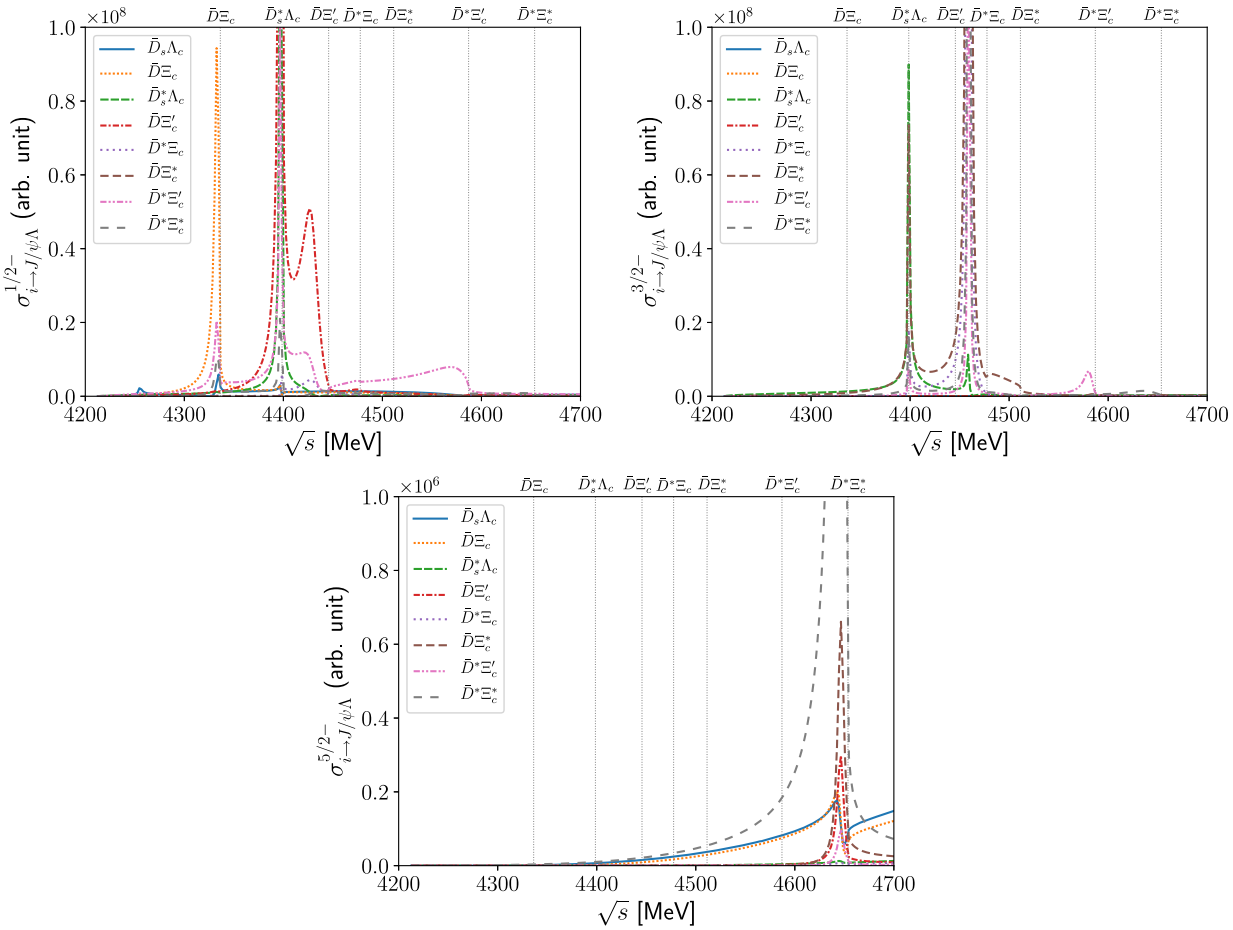


FIG. 4. Partial-wave cross sections for the given total angular momenta $J = 1/2, 3/2, 5/2$ with negative parity, which correspond to the spins and parities of $P_{c\bar{c}s}$, as functions of the total energy.

where two potential peaks appear—a narrow lower structure and a broader higher one. Although these features have not been officially reported as resonances by the LHCb Collaboration, possibly due to limited data or statistical fluctuations, their presence in the data is noticeable and is in agreement with the present theoretical predictions. We expect that future experiments can confirm these structures.

In the $J^P = 3/2^-$ case, depicted in the upper right panel of Fig. 4, we observe a narrow peak below the $\bar{D}^*\Xi_c$ threshold, which can be associated with the $P_{c\bar{c}s}(4459)$ state. Unlike the case of $P_{c\bar{c}}(4440)$ and $P_{c\bar{c}}(4457)$, which have spin-parity assignments of $J^P = 1/2^-$ and $J^P = 3/2^-$, respectively, no corresponding peak structure appears below the $\bar{D}^*\Xi_c$ threshold in the $J^P = 1/2^-$ channel, as shown in the upper left panel of Fig. 4. This suggests that $P_{c\bar{c}s}(4459)$ is composed of a single pole structure. Additionally, we find a peak below the $\bar{D}^*\Xi_c'$ threshold and a broader peak below the $\bar{D}^*\Xi_c^*$ threshold, although their relatively small cross sections may hinder experimental identification. A cusp structure is also visible at the $\bar{D}_s^*\Lambda_c$ threshold. In the $J^P = 5/2^-$ case, shown in the lower panel of Fig. 4, we see only a single narrow peak located just below the $\bar{D}^*\Xi_c^*$ threshold.

To understand these structures, we analyze the pole positions in the second Riemann sheet of the complex energy. All poles found in the negative-parity channel are listed in Table II. We identify eight poles, two of which correspond to the experimentally observed $P_{c\bar{c}s}$ states. The present value for the $P_{c\bar{c}s}(4338)$ mass slightly underestimates the experimental one. For the $P_{c\bar{c}s}(4459)$, the calculation yields a considerably smaller width compared to the experimental result. However, given the present experimental uncertainties, it remains plausible that the actual width of the $P_{c\bar{c}s}(4459)$ is narrower than currently reported. In addition to the known states, we predict six new negative-parity $P_{c\bar{c}s}$ resonances, as well as several nonresonant structures, which may be confirmed by future experimental investigations.

In the following subsection, we provide a detailed analysis of both the known and predicted resonances, as well as the nonresonant structures, by examining the nature of each resonance state. To facilitate this analysis, we calculate the coupling strength of each resonance to the partial-wave components of the relevant two-body states. The coupling strength is extracted from the residue of the transition amplitude, which is expressed as

$$\mathcal{R}_{ab} = \lim_{s\to s_R}(s - s_R)\mathcal{T}_{ab}/4\pi = g_a g_b. \tag{51}$$

We divide the residue by a factor of 4π, since we use a different normalization for the partial-wave decomposition in Eq. (44) from the conventional one based on the Legendre polynomials. Note that the definition of the coupling strength in Eq. (51) does not allow us to determine its absolute sign. To establish the relative signs, thus, we take the real part of the coupling to the lowest threshold channel to be positive. The coupling strengths of each resonance to all relevant channels are listed in Table III. It is essential to know the results for the coupling strengths in Table III, since they will reveal the nature of the hidden-charm pentaquarks with $S = -1$.

1. $P_{c\bar{c}s}(4338)$

The $P_{c\bar{c}s}(4338)$ was first discovered in the $J/\psi\Lambda$ invariant mass spectrum from the decay $B^- \to J/\psi\Lambda\bar{p}$. This state was observed with high statistical significance, allowing for a definitive determination of its spin-parity assignment. Located just below the $\bar{D}\Xi_c$ threshold, it has been widely interpreted in various studies as a molecular state of $\bar{D}\Xi_c$ [12–14,16].

The first resonance listed in Table II is identified with the $P_{c\bar{c}s}(4338)$. We find that the pole corresponding to this state lies approximately 3 MeV below the $\bar{D}\Xi_c$ threshold. When considering only the single $\bar{D}\Xi_c$ channel, it appears as the bound state at about 0.2 MeV below the threshold. We introduce other channels including the $\bar{D}\Xi_c$ one, among which the $\bar{D}\Xi_c$ channel and $\bar{D}^*\Xi_c^*$ channel dominate over all other channels, as shown in Table III. It is interesting to see that even though the $\bar{D}^*\Xi_c^*$ channel has the largest

TABLE II. Pole positions of the hidden-charm pentaquark states with $S = -1$.

		$\sqrt{s_R} = (M - i\Gamma/2)$ MeV		Known states		
J^P	Resonance states	M	Γ	Name	M	Γ
$1/2^-$	$[\bar{D}\Xi_c]_{S=1/2}$	4333.6	4.6	$P_{c\bar{c}s}(4338)$	4338.2 ± 0.8	7.0 ± 1.8
	$[\bar{D}\Xi_c']_{S=1/2}$	4397.8	0.08	…	…	…
	$[\bar{D}\Xi_c']_{S=1/2}$	4429.8	19.9	…	…	…
	$[\bar{D}^*\Xi_c]_{S=1/2}$	4474.9	27.9	$P_{c\bar{c}s}(4472)$	4471.7 ± 4.8	21.9 ± 13.1
$3/2^-$	$[\bar{D}^*\Xi_c]_{S=3/2}$	4459.3	2.0	$P_{c\bar{c}s}(4459)$	$4458.8^{+5.5}_{-3.1}$	17^{+10}_{-9}
	$[\bar{D}^*\Xi_c']_{S=3/2}$	4581.5	10.2	…	…	…
	$[\bar{D}^*\Xi_c^*]_{S=3/2}$	4643.1	39.6	…	…	…
$5/2^-$	$[\bar{D}^*\Xi_c^*]_{S=5/2}$	4646.4	7.6	…	…	…

TABLE III. Coupling strengths of the eight $P_{c\bar{c}s}$'s with $J^P = 1/2^-$, $3/2^-$, and $5/2^-$.

	$1/2^-$			
J^P	$P_{c\bar{c}s}(4338)$	$P_{c\bar{c}s}(4398)$	$P_{c\bar{c}s}(4430)$	$P_{c\bar{c}s}(4472)$
$\sqrt{s_R}$ [MeV]	$4333.6 - i2.3$	$4397.8 - i0.04$	$4429.8 - i10.0$	$4474.9 - i14.0$
$g_{J/\psi\Lambda(^2S_J)}$	$0.08 - i0.02$	$0.1 + i0.01$	$0.04 + i0.1$	$0.03 - i0.01$
$g_{J/\psi\Lambda(^2D_J)}$	…	…	…	…
$g_{J/\psi\Lambda(^4S_J)}$	…	…	…	…
$g_{J/\psi\Lambda(^4D_J)}$	$0.00 - i0.00$	$0.02 + i0.00$	$0.01 - i0.02$	$0.04 - i0.04$
$g_{\bar{D}_s\Lambda_c(^2S_J)}$	$-1.18 - i2.05$	$0.14 + i0.13$	$-0.04 + i0.21$	$0.28 + i0.20$
$g_{\bar{D}_s\Lambda_c(^2D_J)}$	…	…	…	…
$g_{\bar{D}\Xi_c(^2S_J)}$	$9.60 + i2.41$	$0.07 + i0.18$	$-0.08 + i0.20$	$0.20 + i0.29$
$g_{\bar{D}\Xi_c(^2D_J)}$	…	…	…	…
$g_{\bar{D}_s^*\Lambda_c(^2S_J)}$	$-0.27 + i0.05$	$-6.24 - i0.07$	$-0.61 - i5.98$	$4.04 + i1.13$
$g_{\bar{D}_s^*\Lambda_c(^2D_J)}$	…	…	…	…
$g_{\bar{D}_s^*\Lambda_c(^4S_J)}$	…	…	…	…
$g_{\bar{D}_s^*\Lambda_c(^4D_J)}$	$-0.00 + i0.00$	$0.00 + i0.00$	$0.09 - i0.01$	$0.74 + i0.15$
$g_{\bar{D}\Xi_c'(^2S_J)}$	$0.24 - i0.01$	$6.89 + i0.08$	$15.99 + i5.04$	$1.06 + i5.15$
$g_{\bar{D}\Xi_c'(^2D_J)}$	…	…	…	…
$g_{\bar{D}^*\Xi_c(^2S_J)}$	$-0.27 + i0.02$	$0.82 - i0.03$	$-13.72 + i3.56$	$-13.57 - i7.87$
$g_{\bar{D}^*\Xi_c(^2D_J)}$	…	…	…	…
$g_{\bar{D}^*\Xi_c(^4S_J)}$	…	…	…	…
$g_{\bar{D}^*\Xi_c(^4D_J)}$	$-0.01 + i0.00$	$-0.01 + i0.00$	$-0.12 + i0.01$	$-0.01 + i0.04$
$g_{\bar{D}\Xi_c^*(^4S_J)}$	…	…	…	…
$g_{\bar{D}\Xi_c^*(^4D_J)}$	$-0.01 + i0.00$	$0.05 + i0.00$	$-0.07 - i0.04$	$0.01 + i0.01$
$g_{\bar{D}^*\Xi_c'(^2S_J)}$	$-5.78 + i0.90$	$-4.84 - i0.43$	$-8.79 - i4.61$	$-5.38 - i2.19$
$g_{\bar{D}^*\Xi_c'(^2D_J)}$	…	…	…	…
$g_{\bar{D}^*\Xi_c'(^4S_J)}$	…	…	…	…
$g_{\bar{D}^*\Xi_c'(^4D_J)}$	$-0.26 + i0.04$	$0.16 + i0.01$	$-0.24 - i0.14$	$0.10 + i0.06$
$g_{\bar{D}^*\Xi_c^*(^2S_J)}$	$-9.66 + i1.50$	$4.44 - i0.57$	$8.95 + i3.63$	$4.32 + i0.19$
$g_{\bar{D}^*\Xi_c^*(^2D_J)}$	…	…	…	…
$g_{\bar{D}^*\Xi_c^*(^4S_J)}$	…	…	…	…
$g_{\bar{D}^*\Xi_c^*(^4D_J)}$	$0.24 - i0.04$	$0.17 - i0.01$	$-0.31 - i0.15$	$0.11 + i0.04$
$g_{\bar{D}^*\Xi_c^*(^6S_J)}$	…	…	…	…
$g_{\bar{D}^*\Xi_c^*(^6D_J)}$	$0.87 - i0.13$	$0.10 - i0.04$	$0.17 + i0.06$	$0.08 - i0.05$

	$3/2^-$			$5/2^-$
J^P	$P_{c\bar{c}s}(4459)$	$P_{c\bar{c}s}(4582)$	$P_{c\bar{c}s}(4643)$	$P_{c\bar{c}s}(4646)$
$\sqrt{s_R}$ [MeV]	$4459.3 - i1.0$	$4581.5 - i5.1$	$4643.1 - i19.8$	$4646.4 - i3.8$
$g_{J/\psi\Lambda(^2S_J)}$	…	…	…	…
$g_{J/\psi\Lambda(^2D_J)}$	$0.01 + i0.00$	$0.01 - i0.00$	$0.00 + i0.02$	$0.01 + i0.00$
$g_{J/\psi\Lambda(^4S_J)}$	$0.06 + i0.02$	$0.02 - i0.01$	$0.01 - i0.03$	…
$g_{J/\psi\Lambda(^4D_J)}$	$0.06 + i0.01$	$0.03 - i0.02$	$0.03 - i0.06$	$0.03 + i0.00$
$g_{\bar{D}_s\Lambda_c(^2S_J)}$	…	…	…	…
$g_{\bar{D}_s\Lambda_c(^2D_J)}$	$0.03 + i0.00$	$-0.24 - i0.07$	$-0.35 - i0.09$	$-0.38 - i0.12$
$g_{\bar{D}\Xi_c(^2S_J)}$	…	…	…	…
$g_{\bar{D}\Xi_c(^2D_J)}$	$0.03 + i0.00$	$-0.31 - i0.10$	$-0.37 - i0.14$	$-0.54 - i0.21$
$g_{\bar{D}_s^*\Lambda_c(^2S_J)}$	…	…	…	…
$g_{\bar{D}_s^*\Lambda_c(^2D_J)}$	$0.06 - i0.01$	$0.08 + i0.02$	$-0.52 - i0.07$	$0.12 - i0.02$
$g_{\bar{D}_s^*\Lambda_c(^4S_J)}$	$-0.37 - i1.62$	$1.10 + i0.96$	$3.29 + i0.80$	…

(Table continued)

TABLE III. *(Continued)*

	$3/2^-$			$5/2^-$
J^P	$P_{c\bar{c}s}(4459)$	$P_{c\bar{c}s}(4582)$	$P_{c\bar{c}s}(4643)$	$P_{c\bar{c}s}(4646)$
$\sqrt{s_R}$ [MeV]	$4459.3 - i1.0$	$4581.5 - i5.1$	$4643.1 - i19.8$	$4646.4 - i3.8$
$g_{\bar{D}_s^*\Lambda_c(^4D_J)}$	$-0.18 - i0.53$	$0.19 + i0.28$	$0.76 + i0.14$	$-0.17 - i0.02$
$g_{\bar{D}\Xi_c'(^2S_J)}$	…	…	…	…
$g_{\bar{D}\Xi_c'(^2D_J)}$	$0.06 - i0.03$	$1.58 + i0.53$	$-0.07 + i0.01$	$-1.03 - i0.27$
$g_{\bar{D}^*\Xi_c(^2S_J)}$	…	…	…	…
$g_{\bar{D}^*\Xi_c(^2D_J)}$	$0.02 + 0.00$	$0.25 - i0.05$	$-0.65 - i0.25$	$0.11 + i0.09$
$g_{\bar{D}^*\Xi_c(^4S_J)}$	$-15.07 + i0.76$	$0.67 + i1.08$	$2.35 + i1.09$	…
$g_{\bar{D}^*\Xi_c(^4D_J)}$	$-5.05 + i0.26$	$0.32 + i0.24$	$0.48 + i0.16$	$-0.13 - i0.11$
$g_{\bar{D}\Xi_c^*(^4S_J)}$	$-14.75 - i2.00$	$-2.00 + i0.11$	$-3.51 + i1.26$	…
$g_{\bar{D}\Xi_c^*(^4D_J)}$	$-4.98 - i0.68$	$-1.97 + i0.35$	$1.06 + i1.43$	$-2.13 - i0.35$
$g_{\bar{D}^*\Xi_c'(^2S_J)}$	…	…	…	…
$g_{\bar{D}^*\Xi_c'(^2D_J)}$	$-0.06 - i0.01$	$0.00 + i0.10$	$-0.96 + i0.58$	$0.66 - i0.07$
$g_{\bar{D}^*\Xi_c'(^4S_J)}$	$5.87 + i0.81$	$-13.37 - i3.54$	$2.34 - i0.25$	…
$g_{\bar{D}^*\Xi_c'(^4D_J)}$	$2.03 + i0.28$	$-4.46 - i1.20$	$0.78 - i0.39$	$-0.85 + i0.09$
$g_{\bar{D}^*\Xi_c^*(^2S_J)}$	…	…	…	…
$g_{\bar{D}^*\Xi_c^*(^2D_J)}$	$0.76 + i0.11$	$0.04 - i0.23$	$1.05 + i0.44$	$1.83 + i0.36$
$g_{\bar{D}^*\Xi_c^*(^4S_J)}$	$11.37 + i1.57$	$0.56 - i4.00$	$-19.92 - i7.57$	…
$g_{\bar{D}^*\Xi_c^*(^4D_J)}$	$3.60 + i0.49$	$0.19 - i1.30$	$-6.62 - 2.49i$	$-0.00 - i0.00$
$g_{\bar{D}^*\Xi_c^*(^6S_J)}$	…	…	…	$14.09 + i2.77$
$g_{\bar{D}^*\Xi_c^*(^6D_J)}$	$0.09 + i0.01$	$0.02 - i0.01$	$0.00 + i0.03$	$6.29 + i1.25$

threshold energy, it still influences the generation of the $P_{c\bar{c}s}(4338)$ state as a resonance. Consequently, the pole moves to the second Riemann sheet, such that it arises as the resonance. $P_{c\bar{c}s}(4338)$ is strongly coupled to both the $\bar{D}\Xi_c$ channel and $\bar{D}^*\Xi_c^*$ channel. Note that the $\bar{D}^*\Xi_c'$ channel has a sizable contribution to the $P_{c\bar{c}s}(4338)$ state. Though the $P_{c\bar{c}s}(4338)$ pentaquark state observed by the LHCb Collaboration is positioned slightly above the $\bar{D}\Xi_c$ threshold, the present result implies that the $P_{c\bar{c}s}(4338)$ can be considered to be a $\bar{D}\Xi_c$ bound state, based on the present calculation.

2. $P_{c\bar{c}s}(4459)$

Concerning the $P_{c\bar{c}s}(4459)$, the LHCb and Belle data show slight discrepancies. The LHCb Collaboration reported its mass as $(4458.8 \pm 2.9^{+4.7}_{-1.1})$ MeV with a width of $\Gamma = (17.3 \pm 6.5^{+8.0}_{-5.7})$ MeV, while the Belle Collaboration measured the mass to be $(4471.7 \pm 4.8 \pm 0.6)$ MeV and the width as $\Gamma = (21.9 \pm 13.1 \pm 2.7)$ MeV. Interestingly, we found two $P_{c\bar{c}s}$ states that correspond to those reported by the LHCb and Belle collaborations, respectively. These states are located below the $\bar{D}^*\Xi_c$ threshold, as shown in Fig. 1 and Table III. Their masses and widths are obtained to be $M_{P_{c\bar{c}s}(4459)} = 4459.3$ MeV and $\Gamma_{P_{c\bar{c}s}(4459)} = 2$ MeV, and $M_{P_{c\bar{c}s}(4472)} = 4474.9$ MeV and $\Gamma_{P_{c\bar{c}s}(4472)} = 28$ MeV, respectively. This indicates that not only the masses but also the widths are comparable to the experimental data. Based on the predictions of the present work, we suggest that the $P_{c\bar{c}s}$ state identified by the LHCb Collaboration should be distinguished from the one reported by the Belle Collaboration. We therefore conclude that there exist *two* hidden-charm pentaquark states with $S = -1$ below the $\bar{D}^*\Xi_c$ threshold.

Though these two pentaquark states are positioned very close each other, their spins are different. While the $P_{c\bar{c}s}(4459)$ has spin $3/2$, the $P_{c\bar{c}s}(4472)$ has spin $1/2$. Their parities are negative. It means that these two poles are the separate resonances without any two-pole structure. As mentioned above, these two pentaquark states lie below the $\bar{D}^*\Xi_c$ threshold. Thus, both the resonances may be considered as molecular states consisting of the $\bar{D}^*$ with $I(J^P) = 1/2(1^-)$ and Ξ_c with $J^P = 1/2(1/2)^+$. To understand this nature, we need to examine how these two pentaquark states arise from the coupled-channel interactions.

As demonstrated in Fig. 5, the single-channel $\bar{D}^*\Xi_c$ interaction generates threshold enhancements in both the $J^P = 1/2^-$ and $3/2^-$ channels. When coupled to other channels, these enhancements evolve into the broad $P_{c\bar{c}s}(4475)$ and the narrow $P_{c\bar{c}s}(4459)$ states. As shown in Table III, the broad $P_{c\bar{c}s}(4475)$ couples most strongly to the $\bar{D}^*\Xi_c$ channel, with the magnitude of the corresponding coupling strength approximately ten times larger than its

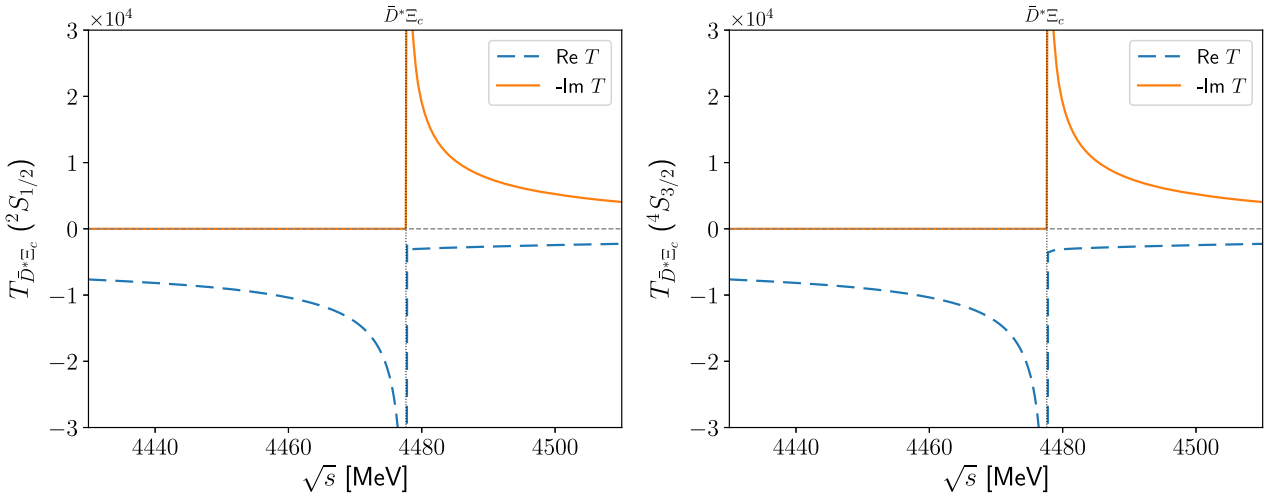


FIG. 5. Invariant $\mathcal{T}$ amplitudes for $\bar{D}\Xi_c'$ elastic scattering with both spin $1/2^-$ and $3/2^-$ as functions of the total energy. generated by the single $\bar{D}^*\Xi_c$ channel for $J^P = 1/2^-$ (left panel) and $J^P = 3/2^-$ (right panel).

next strongest coupling. In contrast, the narrow $P_{c\bar{c}s}(4459)$ state, while also coupling most strongly to the $\bar{D}^*\Xi_c$ channel, exhibits a coupling strength comparable to that to the $\bar{D}\Xi_c^*$ channel. We find that this crucial interplay between the coupling strengths causes an interesting feature: the higher-mass pole $P_{c\bar{c}s}(4472)$ is overshadowed by the presence of the narrower state, $P_{c\bar{c}s}(4459)$. Comparing the upper left panel of Fig. 4 with its upper right panel, one can see this feature. Although the patterns of the coupling strengths for the $P_{c\bar{c}s}(4459)$ and $P_{c\bar{c}s}(4472)$ turn out to be different, the dominant role of the $\bar{D}^*\Xi_c$ channel in both cases implies that both the $P_{c\bar{c}s}(4459)$ and $P_{c\bar{c}s}(4475)$ can be regarded as $\bar{D}^*\Xi_c$ molecular states.

3. Two resonances in the $\bar{D}\Xi_c'$ channel

Notably, the $P_{c\bar{c}s}(4398)$ peak almost overlaps with the $\bar{D}_s^*\Lambda_c$ threshold ($E_{\text{th}} \approx 4398$ MeV). The width of the $P_{c\bar{c}s}(4398)$ is extremely narrow—less than 1 MeV—placing it very close to the real energy axis. This suggests that the $P_{c\bar{c}s}(4398)$ may be an almost bound state of $\bar{D}_s^*$ and Λ_c. On the other hand, the $P_{c\bar{c}s}(4430)$ lies between the $\bar{D}_s^*\Lambda_c$ and $\bar{D}\Xi_c'$ thresholds, as shown in Fig. 1. Therefore, to determine whether the $P_{c\bar{c}s}(4430)$ is a molecular state of $\bar{D}$ and Ξ_c', it is necessary to examine its coupling strengths to various channels in detail.

In Fig. 6, we show that the $\bar{D}\Xi_c'$ single channel generates a bound state. As additional channels are introduced, this bound state acquires a finite width and eventually evolves into the $P_{c\bar{c}s}(4430)$ resonance. As shown in Table III, four different channels contribute to the generation of the $P_{c\bar{c}s}(4430)$: the $\bar{D}\Xi_c'$, $\bar{D}^*\Xi_c$, $\bar{D}^*\Xi_c^*$, and $\bar{D}^*\Xi_c'$ channels, among which the $\bar{D}\Xi_c'$ channel is the most strongly coupled. Therefore, we may regard the $P_{c\bar{c}s}(4430)$ as a molecular state composed of a $\bar{D}$ meson and a Ξ_c' baryon.

When all other channels are introduced, the $P_{c\bar{c}s}(4398)$ emerges as a second state, located almost exactly at the $\bar{D}_s^*\Lambda_c$ threshold. This proximity suggests that it may be interpreted as a $\bar{D}_s^*\Lambda_c$ bound state. To investigate its nature, we examine the scattering amplitude generated by the $\bar{D}_s^*\Lambda_c$ single channel. Interestingly, no bound state is found below its threshold. This result implies that the $P_{c\bar{c}s}(4398)$ cannot be interpreted as a pure $\bar{D}\Xi_c'$ or $\bar{D}_s^*\Lambda_c$ molecular state.

As listed in Table III, four channels are dominantly coupled to the $P_{c\bar{c}s}(4398)$: the $\bar{D}\Xi_c'$, $\bar{D}_s^*\Lambda_c$, $\bar{D}^*\Xi_c'$, and $\bar{D}^*\Xi_c^*$ channels. These are the same channels that dominantly contribute to the $P_{c\bar{c}s}(4430)$ as well. This indicates that the would-be single pole appearing in the $\bar{D}\Xi_c'$ single

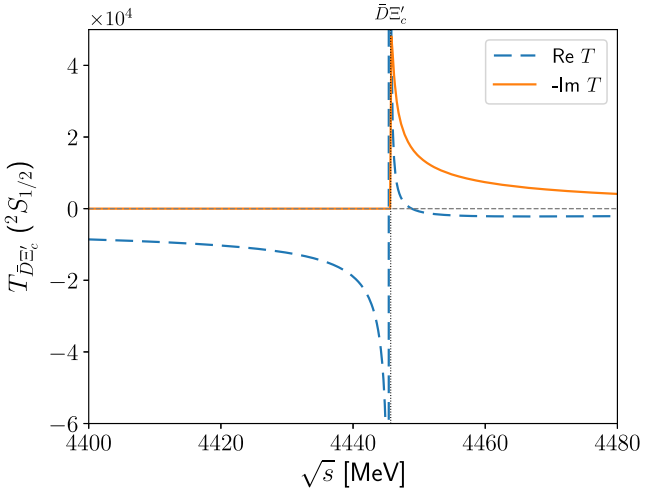


FIG. 6. Invariant $\mathcal{T}$ amplitude for $\bar{D}\Xi_c'$ elastic scattering with $J^P = 1/2^-$ as a function of the total energy. Note that only the single $\bar{D}\Xi_c'$ channel is considered.

channel becomes split into two hidden-charm pentaquark states with strangeness $S = -1$ due to the interplay of the four aforementioned channels. This behavior is reminiscent of a possible two-pole structure.

These two peaks bear a resemblance to the well-known two-pole structure of the $\Lambda(1405)$ [43,44]. A similar structure was also observed in the dynamical generation of the $b_1(1235)$ axial-vector meson in a previous work [45]. Moreover, the two-pole structure of the $h_1(1415)$ provides a natural explanation for the conflicting mass values reported by several experiments for this state [46]. These observations are not unexpected, as the two-pole structure is a general feature that arises in the dynamical generation of resonances via hadron-hadron interactions (see Ref. [47] for a detailed discussion). Therefore, it is of great interest to identify this structure experimentally.

4. A resonance in the $\bar{D}^*\Xi_c'$ channel

In the upper left panel of Fig. 4, below the $\bar{D}^*\Xi_c'$ threshold, we observe a broad peak in the $\bar{D}^*\Xi_c' \to J/\psi\Lambda$ transition, which could be misinterpreted as a resonance state. This is confirmed in Table II, where no pole with $J^P = 1/2^-$ is found just below the $\bar{D}^*\Xi_c'$ threshold. Therefore, this broad peak does not correspond to a pole on the second Riemann sheet. Instead, it originates from a virtual state near the $\bar{D}^*\Xi_c'$ threshold that affects the physical energy axis. In contrast, the peak structure in the same transition channel with $J^P = 3/2^-$ corresponds to a genuine resonance, with a mass of 4581.5 MeV and a width of 10.2 MeV. Although this state has not yet been experimentally found, it is possible to observe it in the $\Xi_b^- \to J/\psi\Lambda K^-$ decay channel.

We calculate the scattering amplitude from the $\bar{D}^*\Xi_c'$ single channel with $J^P = 1/2^-$ and $3/2^-$, and find that each produces a bound state below its threshold. However, after coupling to all other channels, only the bound state with $J^P = 3/2^-$ arises as a resonance state, while the $J^P = 1/2^-$ state becomes virtual. This phenomenon also appears in our previous work, specifically where the $\bar{D}^*\Sigma_c^*$ molecular state with $J^P = 1/2^-$ similarly becomes a virtual state due to coupled-channel effects [21]. Therefore, it is crucial to consider all possible coupled channels when constructing the transition amplitudes. Moreover, these results demonstrate the inadequacy of considering symmetry alone while neglecting the underlying dynamics.

5. Resonances in the $\bar{D}^*\Xi_c^*$ channel

The present analysis reveals two additional states that have not yet been experimentally observed, both appearing near the $\bar{D}^*\Xi_c^*$ threshold: $P_{c\bar{c}s}(4643)$ and $P_{c\bar{c}s}(4646)$, with spin-parity assignments of $3/2^-$ and $5/2^-$, respectively. The lower-mass state exhibits a broader width than its higher-mass counterpart, and together they generate the structure observed below the $\bar{D}^*\Xi_c^*$ threshold in the $\bar{D}^*\Xi_c^* \to J/\psi\Lambda$ transition. Notably, no pole is found below this threshold in the $J^P = 1/2^-$ channel. A pattern also is seen previously in the $\bar{D}^*\Xi_c'$ channel and in the $\bar{D}^*\Sigma_c^*$ molecular case discussed in our earlier work [21]. As shown in the upper right and lower panels of Fig. 4, these resonances produce significantly smaller cross sections compared to the other states discussed earlier, making them barely visible.

To further investigate this phenomenon, we examine the transition amplitude constructed from the $\bar{D}^*\Xi_c^*$ single channel for different total spin states. We identify bound states below the $\bar{D}^*\Xi_c^*$ threshold with $J^P = 1/2^-$, $3/2^-$, and $5/2^-$. Upon coupling to all other channels, all of these bound states evolve into resonances, except the one with $J^P = 1/2^-$. The $J^P = 3/2^-$ and $5/2^-$ states are identified as the $P_{c\bar{c}s}(4643)$ and $P_{c\bar{c}s}(4646)$ resonances, respectively, as shown in Table III. Both the resonances couple most strongly to the $\bar{D}^*\Xi_c^*$ channel. The broader width of the lower-mass state can be attributed to its coupling to a larger number of channels. Based on these coupling patterns, we conclude that both resonances are molecular states of $\bar{D}^*\Xi_c^*$.

6. Cusps in the $\bar{D}_s\Lambda_c$ and $\bar{D}_s^*\Lambda_c$ threshold

In addition to resonance and virtual states, the current formalism also allows for the identification of cusp structures. Figure 7, which presents an enlarged view of the upper left panel of Fig. 4 around 4.25 GeV, reveals a cusp at the $\bar{D}_s\Lambda_c$ threshold. This cusp is particularly noteworthy, as it might correspond to the narrow peak observed near the $\bar{D}_s\Lambda_c$ threshold in the $J/\psi\Lambda$ invariant mass distribution from the $B^- \to J/\psi\Lambda\bar{p}$ decay reported in Ref. [4], where the interpretation as a resonance state suffers from lacked statistical significance. The cusp originates from the $\bar{D}_s\Lambda_c$ single channel, which alone cannot generate a bound state.

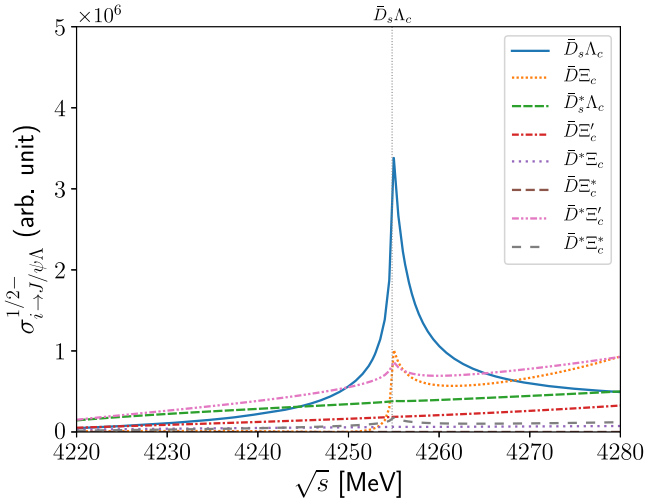


FIG. 7. Enlarged view of the upper left panel of Fig. 4 around 4.25 GeV.

The coupled-channel dynamics merely enhance this threshold effect, leading to a cusp structure rather than a true resonance.

Another significant cusp appears in the $J^P = 3/2^-$ channel at the $\bar{D}_s^*\Lambda_c$ threshold, as shown in the upper right panel of Fig. 4. Although this cusp has an intensity comparable to that of the $P_{c\bar{c}s}(4338)$ peak, it is obscured by the nearby $P_{c\bar{c}s}(4398)$ resonance. Its identification would therefore require a detailed amplitude analysis.

B. Positive parity

The positive-parity states generated in the current work demonstrate its ability to produce resonances through P-wave interactions. Figure 8 presents the partial-wave cross sections for transitions from various initial states to $J/\psi\Lambda$ with $J^P = 1/2^+$, $3/2^+$, and $5/2^+$. In the $J^P = 1/2^+$ channel (upper left panel), we observe two peak structures: one located between the $\bar{D}\Xi_c^*$ and $\bar{D}^*\Xi_c'$ thresholds, which is clearly visible in the $\bar{D}\Xi_c^* \to J/\psi\Lambda$ transition, and another near the $\bar{D}^*\Xi_c^*$ threshold, which is evident in the $\bar{D}_s^*\Lambda_c \to J/\psi\Lambda$ transition channel. However, compared to their negative-parity counterparts, these peaks exhibit smaller cross sections, indicating that it may be rather difficult to detect them experimentally.

The $J^P = 3/2^+$ channel, shown in the upper right panel of Fig. 8, exhibits a distinct peak near the $\bar{D}^*\Xi_c'$ threshold, which is clearly visible in two transition channels: $\bar{D}_s\Lambda_c \to J/\psi\Lambda$ and $\bar{D}\Xi_c \to J/\psi\Lambda$. Additionally, a less-prominent bump is observed around the $\bar{D}^*\Xi_c^*$ threshold. In the lower panel of Fig. 8, the $J^P = 5/2^+$ channel shows no significant peak structures. A characteristic feature of these positive-parity cases is the relatively modest threshold effects, with most peak structures emerging approximately at their corresponding thresholds, rather than significantly above or below them, in contrast to the behavior found in the negative-parity channels.

Among the three peaks and one bump observed in the $J^P = 1/2^+$ and $3/2^+$ channels, we identify three corresponding poles, with their positions and coupling strengths to all channels listed in Table IV. The first pole, $P_{c\bar{c}s}(4534)$, which generates the initial peak structure in the upper panel of Fig. 8, couples most strongly to the $\bar{D}\Xi_c^*$ channel. Notably, it does not couple to channels with thresholds above its mass, in stark contrast to the negative-parity cases, where dynamically generated poles typically exhibit

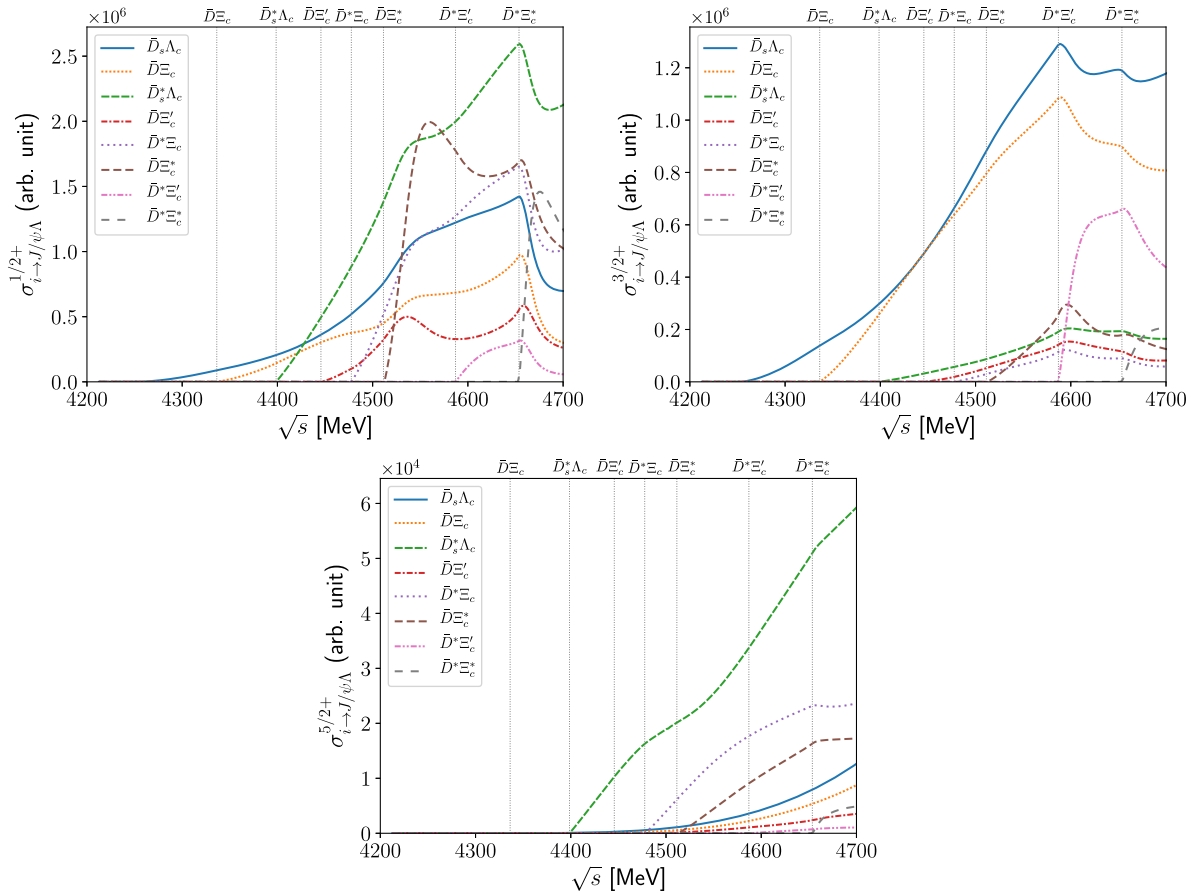


FIG. 8. Total energy dependence of the partial-wave total cross sections for positive-parity states ($J = 1/2, 3/2, 5/2$) corresponding to the spin-parity quantum numbers of $P_{c\bar{c}s}$.

TABLE IV. Coupling strengths of $P_{c\bar{c}s}$'s with $J^P = 1/2^+$ and $3/2^+$.

J^P	$1/2^+$		$3/2^+$
$\sqrt{s_R}$ [MeV]	$4533.7 - i32.4$	$4658.2 - i17.2$	$4588.9 - i20.6$
$g_{J/\psi\Lambda(^2P_J)}$	$0.01 + i0.00$	$0.09 + i0.02$	$0.02 - i0.01$
$g_{J/\psi\Lambda(^4P_J)}$	$0.21 - i0.10$	$0.16 + i0.03$	$0.04 - i0.00$
$g_{J/\psi\Lambda(^4F_J)}$	…	…	$0.03 - i0.00$
$g_{\bar{D}_s\Lambda_c(^2P_J)}$	$0.02 - i0.55$	$-0.82 + i0.34$	$0.83 - i0.44$
$g_{\bar{D}\Xi_c(^2P_J)}$	$0.22 - i0.62$	$-0.96 + i0.44$	$0.86 - i0.46$
$g_{\bar{D}_s^*\Lambda_c(^2P_J)}$	$-0.72 + i0.52$	$-0.88 + i0.61$	$0.03 - i0.27$
$g_{\bar{D}_s^*\Lambda_c(^4P_J)}$	$-1.02 + i1.01$	$-0.56 + i0.42$	$-0.54 + i0.83$
$g_{\bar{D}_s^*\Lambda_c(^4F_J)}$	…	…	$-0.53 + i0.43$
$g_{\bar{D}\Xi_c'(^2P_J)}$	$2.75 - i0.35$	$1.05 + i0.69$	$0.40 - i0.07$
$g_{\bar{D}^*\Xi_c(^2P_J)}$	$0.47 + i1.07$	$-1.38 + i0.53$	$-0.13 + i0.13$
$g_{\bar{D}^*\Xi_c(^4P_J)}$	$-0.75 + i1.90$	$-0.91 + i0.41$	$-1.27 + i0.86$
$g_{\bar{D}^*\Xi_c(^4F_J)}$	…	…	$-1.69 + i0.25$
$g_{\bar{D}\Xi_c^*(^4P_J)}$	$-3.48 + i6.22$	$-0.91 - i0.44$	$-2.81 - i0.43$
$g_{\bar{D}\Xi_c^*(^4F_J)}$	…	…	$-0.02 - i1.87$
$g_{\bar{D}^*\Xi_c'(^2P_J)}$	$0.00 + i0.00$	$-1.44 + i0.31$	$-0.43 + i4.33$
$g_{\bar{D}^*\Xi_c'(^4P_J)}$	$0.00 + i0.00$	$-0.17 + i0.87$	$5.86 - i4.39$
$g_{\bar{D}^*\Xi_c'(^4F_J)}$	…	…	$3.20 - i3.12$
$g_{\bar{D}^*\Xi_c^*(^2P_J)}$	$0.00 + i0.00$	$3.10 - i6.75$	$0.00 + i0.00$
$g_{\bar{D}^*\Xi_c^*(^4P_J)}$	$0.00 + i0.00$	$1.99 - i2.61$	$0.00 + i0.00$
$g_{\bar{D}^*\Xi_c^*(^4F_J)}$	…	…	$0.00 + i0.00$
$g_{\bar{D}^*\Xi_c^*(^6P_J)}$	…	…	$0.00 + i0.00$
$g_{\bar{D}^*\Xi_c^*(^6F_J)}$	$0.00 + i0.01$	$0.83 - i0.51$	$0.00 + i0.00$

significant couplings to higher-threshold channels. These characteristics suggest that the positive-parity hidden-charm pentaquark states may originate from *genuine* pentaquark states or could merely reflect coupled-channel effects.

The second pole, $P_{c\bar{c}s}(4658)$, responsible for the second peak structure, lies above the highest threshold and couples to all accessible channels. It exhibits the strongest coupling to the $\bar{D}^*\Xi_c^*$ channel, particularly in the $^2P_{1/2}$ partial wave.

A unique feature of the singly strange hidden-charm pentaquark system, in contrast to the $P_{c\bar{c}}$ case discussed in our previous work [21], is the presence of a resonance with $J^P = 3/2^+$. This pole generates the peak structure near the $\bar{D}^*\Xi_c'$ threshold and couples most strongly to the $^4P_{3/2}$ wave of the $\bar{D}^*\Xi_c'$ state, while exhibiting no coupling to the $\bar{D}^*\Xi_c^*$ channel.

IV. SUMMARY AND CONCLUSIONS

In this work, we have investigated the molecular nature of singly strange hidden-charm pentaquark states, $P_{c\bar{c}s}$, using an off shell coupled-channel formalism based on effective Lagrangians that respect heavy-quark spin symmetry, SU(3) flavor symmetry, and hidden local symmetry. We included all relevant two-body channels composed of ground-state anticharmed mesons and singly charmed baryons with strangeness $S = -1$, along with the $J/\psi\Lambda$ channel.

Solving the coupled-channel scattering equations, we identified eight negative-parity resonances—four with $J^P = 1/2^-$, three with $J^P = 3/2^-$, and one with $J^P = 5/2^-$—as well as three positive-parity states. Among these, the $P_{c\bar{c}s}(4338)$ and $P_{c\bar{c}s}(4459)$ can be associated with experimentally observed pentaquark candidates. We have analyzed their strong couplings to specific meson-baryon channels and interpreted them as hadronic molecules: the $P_{c\bar{c}s}(4338)$ as a predominantly $\bar{D}\Xi_c$ bound state, and the $P_{c\bar{c}s}(4459)$ as a $\bar{D}^*\Xi_c$ molecular resonance with $J^P = 3/2^-$.

A particularly important result is the identification of the $P_{c\bar{c}s}(4472)$, located close to the $P_{c\bar{c}s}(4459)$ but with a larger width and a different spin-parity assignment. Both originate from the same $\bar{D}^*\Xi_c$ single channel, with $J^P = 3/2^-$ for the $P_{c\bar{c}s}(4459)$ and $J^P = 1/2^-$ for the $P_{c\bar{c}s}(4472)$. This implies that the two observed structures in the vicinity of 4.46 GeV can be understood as spin-partner states dynamically generated by the same interaction kernel. The narrow width and strong coupling of the $P_{c\bar{c}s}(4459)$ to the $J/\psi\Lambda$ channel are consistent with the recent observation by LHCb, while the broader $P_{c\bar{c}s}(4472)$ is potentially relevant for the structure reported by the Belle Collaboration. These findings strongly support the molecular interpretation of the observed $P_{c\bar{c}s}$ candidates.

On the other hand, the two resonances $P_{c\bar{c}s}(4398)$ and $P_{c\bar{c}s}(4430)$, located near the $\bar{D}_s^*\Lambda_c$ and $\bar{D}\Xi_c'$ thresholds, respectively, show signatures of a two-pole behavior. This phenomenon is reminiscent of the well-known $\Lambda(1405)$ and other mesonic states such as the $b_1(1235)$ and $h_1(1415)$, where two poles emerge due to channel coupling. The $P_{c\bar{c}s}(4398)$ lies extremely close to the real axis with a narrow width, while the $P_{c\bar{c}s}(4430)$ appears as a broader resonance. Our analysis of the scattering amplitudes and channel couplings indicates that both states originate from a single-channel pole in the $\bar{D}\Xi_c'$ system, which splits due to the dynamical effects of other channels.

We also analyzed virtual state effects, particularly in the $J^P = 1/2^-$ channel of the $\bar{D}^*\Xi_c'$ system, where no physical pole was found despite a visible enhancement near threshold. In contrast, a genuine resonance with $J^P = 3/2^-$ and mass 4581.5 MeV was identified in the same channel. This resonance is predicted to be detectable in the $\Xi_b^- \to J/\psi\Lambda K^-$ decay, as its cross section, while small, remains detectable.

While we considered the $P_{c\bar{c}s}$ resonances with negative parity as molecular states, there is a caveat. To underpin the molecular nature of these resonances, one must carefully study their decay modes and other physical properties. We will leave it as a future work.

We can also extend the current formalism to investigate the $S = -2$ hidden-charm pentaquark states. This will

involve the charmed mesons with strangeness $S = 0$ and -1, together with the singly charmed baryons with $S = -1$ and -2, so that we can construct the two-body meson-baryon scattering amplitudes with $S = -2$. The corresponding work is under way.

ACKNOWLEDGMENTS

The present work was supported by the Young Scientist Training (YST) Program at the Asia Pacific Center for Theoretical Physics (APCTP) through the Science and Technology Promotion Fund and Lottery Fund of the Korean Government and also by the Korean Local Governments–Gyeongsangbuk-do Province and Pohang City (S. C.), the Basic Science Research Program through the National Research Foundation of Korea funded by the Korean government (Ministry of Education, Science and Technology, MEST), Grant No. RS-2025-00513982 (H.-C. K.), and the PUTI Q1 Grant from University of Indonesia under Contract No. NKB-441/UN2.RST/HKP.05.00/2024 (T. M.).

DATA AVAILABILITY

The data are not publicly available. The data are available from the authors upon reasonable request.

[1] R. Aaij *et al.* (LHCb Collaboration), Phys. Rev. Lett. **115**, 072001 (2015).
[2] R. Aaij *et al.* (LHCb Collaboration), Phys. Rev. Lett. **122**, 222001 (2019).
[3] R. Aaij *et al.* (LHCb Collaboration), Phys. Rev. Lett. **128**, 062001 (2022).
[4] R. Aaij *et al.* (LHCb Collaboration), Phys. Rev. Lett. **131**, 031901 (2023).
[5] I. Adachi *et al.* (Belle Collaboration and Belle II Collaboration), arXiv:2502.09951.
[6] A. Hayrapetyan *et al.* (CMS Collaboration), Eur. Phys. J. C **84**, 1062 (2024).
[7] R. Aaij *et al.* (LHCb Collaboration), arXiv:2501.12779.
[8] J.-J. Wu, R. Molina, E. Oset, and B. S. Zou, Phys. Rev. Lett. **105**, 232001 (2010).
[9] C. W. Xiao, J. Nieves, and E. Oset, Phys. Lett. B **799**, 135051 (2019).
[10] B. Wang, L. Meng, and S.-L. Zhu, Phys. Rev. D **101**, 034018 (2020).
[11] M.-L. Du, Z.-H. Guo, and J. A. Oller, Phys. Rev. D **104**, 114034 (2021).
[12] M. Karliner and J. L. Rosner, Phys. Rev. D **106**, 036024 (2022).
[13] A. Giachino, A. Hosaka, E. Santopinto, S. Takeuchi, M. Takizawa, and Y. Yamaguchi, Phys. Rev. D **108**, 074012 (2023).
[14] F.-L. Wang and X. Liu, Phys. Lett. B **835**, 137583 (2022).
[15] M.-J. Yan, F.-Z. Peng, M. Sánchez Sánchez, and M. Pavon Valderrama, Phys. Rev. D **107**, 074025 (2023).
[16] J.-T. Zhu, S.-Y. Kong, and J. He, Phys. Rev. D **107**, 034029 (2023).
[17] P.-P. Shi, F. Huang, and W.-L. Wang, Eur. Phys. J. A **57**, 237 (2021).
[18] S.-Y. Li, Y.-R. Liu, Z.-L. Man, Z.-G. Si, and J. Wu, Phys. Rev. D **108**, 056015 (2023).
[19] W.-X. Zhang, C.-L. Liu, and D. Jia, Phys. Rev. D **109**, 114037 (2024).
[20] T. J. Burns and E. S. Swanson, Phys. Lett. B **838**, 137715 (2023).
[21] S. Clymton, H.-C. Kim, and T. Mart, Phys. Rev. D **110**, 094014 (2024).
[22] A. Ali *et al.* (GlueX Collaboration), Phys. Rev. Lett. **123**, 072001 (2019).
[23] R. Blankenbecler and R. Sugar, Phys. Rev. **142**, 1051 (1966).
[24] R. Aaron, R. D. Amado, and J. E. Young, Phys. Rev. **174**, 2022 (1968).
[25] R. Casalbuoni, A. Deandrea, N. Di Bartolomeo, R. Gatto, F. Feruglio, and G. Nardulli, Phys. Rep. **281**, 145 (1997).
[26] C. Isola, M. Ladisa, G. Nardulli, and P. Santorelli, Phys. Rev. D **68**, 114001 (2003).
[27] K. Kawarabayashi and M. Suzuki, Phys. Rev. Lett. **16**, 255 (1966).
[28] Riazuddin and Fayyazuddin, Phys. Rev. **147**, 1071 (1966).
[29] W. A. Bardeen, E. J. Eichten, and C. T. Hill, Phys. Rev. D **68**, 054024 (2003).
[30] Y.-R. Liu and M. Oka, Phys. Rev. D **85**, 014015 (2012).
[31] T.-M. Yan, H.-Y. Cheng, C.-Y. Cheung, G.-L. Lin, Y. C. Lin, and H.-L. Yu, Phys. Rev. D **46**, 1148 (1992); **55**, 5851(E) (1997).
[32] R. Chen, Z.-F. Sun, X. Liu, and S.-L. Zhu, Phys. Rev. D **100**, 011502 (2019).
[33] X.-K. Dong, F.-K. Guo, and B.-S. Zou, Prog. Phys. **41**, 65 (2021).
[34] P. Colangelo, F. De Fazio, and T. N. Pham, Phys. Rev. D **69**, 054023 (2004).
[35] R. Casalbuoni, A. Deandrea, N. Di Bartolomeo, R. Gatto, F. Feruglio, and G. Nardulli, Phys. Lett. B **309**, 163 (1993).
[36] Y. Shimizu and M. Harada, Phys. Rev. D **96**, 094012 (2017).
[37] H.-C. Kim, J. W. Durso, and K. Holinde, Phys. Rev. C **49**, 2355 (1994).
[38] J.-Y. Kim and H.-C. Kim, Phys. Rev. D **97**, 114009 (2018).
[39] J.-Y. Kim, H.-C. Kim, G.-S. Yang, and M. Oka, Phys. Rev. D **103**, 074025 (2021).
[40] M. I. Haftel and F. Tabakin, Nucl. Phys. **A158**, 1 (1970).
[41] R. Machleidt, K. Holinde, and C. Elster, Phys. Rep. **149**, 1 (1987).

[42] R. Aaij *et al.* (LHCb Collaboration), Sci. Bull. **66**, 1278 (2021).
[43] J. A. Oller and U. G. Meissner, Phys. Lett. B **500**, 263 (2001).
[44] D. Jido, J. A. Oller, E. Oset, A. Ramos, and U. G. Meissner, Nucl. Phys. **A725**, 181 (2003).
[45] S. Clymton and H.-C. Kim, Phys. Rev. D **108**, 074021 (2023).
[46] S. Clymton and H.-C. Kim, Phys. Rev. D **110**, 114002 (2024).
[47] U.-G. Meißner, Symmetry **12**, 981 (2020).